

## How Gas Accretion Feeds Galactic Disks

STEPHANIE H. HO,<sup>1</sup> CRYSTAL L. MARTIN,<sup>1</sup> AND MONICA L. TURNER<sup>2</sup><sup>1</sup>*Department of Physics, University of California, Santa Barbara, CA 93106, USA*<sup>2</sup>*Las Cumbres Observatory, 6740 Cortona Drive, Goleta, CA 93117, USA*

## ABSTRACT

Numerous observations indicate that galaxies need a continuous gas supply to fuel star formation and explain the star formation history. However, direct observational evidence of gas accretion remains rare. Using the **EAGLE** cosmological hydrodynamic simulation suite, we study cold gas accretion onto galaxies and the observational signatures of the cold gas kinematics. For **EAGLE** galaxies at  $z = 0.27$ , we find that cold gas accretes onto galaxies anisotropically with typical inflow speeds between  $20 \text{ km s}^{-1}$  and  $60 \text{ km s}^{-1}$ . Most of these galaxies have comparable mass inflow rates and star formation rates, implying that the cold inflowing gas plausibly accounts for sustaining the star-forming activities of the galaxies. As motivation for future work to compare the cold gas kinematics with measurements from quasar sightline observations, we select an **EAGLE** galaxy with an extended cold gas disk, and we probe the cold gas using mock quasar sightlines. We demonstrate that by viewing the disk edge-on, sightlines at azimuthal angles below  $10^\circ$  and impact parameters out to  $60 \text{ pkpc}$  can detect cold gas that corotates with the galaxy disk. This example suggests cold gas disks that extend beyond the optical disks possibly explain the sightline observations that detect corotating cold gas near galaxy major axes.

*Keywords:* galaxies: evolution, galaxies: formation, galaxies: halos, (galaxies:) quasars: absorption lines

## 1. INTRODUCTION

Observations have indicated the need for gas accretion onto galaxies. Infalling gas prolongs the gas consumption times of galaxies, or else the star formation of galaxies would exhaust the gas within a few gigayears (Gyrs) (Bigiel et al. 2008, 2011; Leroy et al. 2008, 2013; Rahman et al. 2012). Gas infall helps regulate galaxy star formation and is responsible for the color of galaxy disks along the Hubble sequence (Kennicutt 1998). Continuous accretion of metal-poor gas explains the relative paucity of low metallicity stars in the disk, known as the G-dwarf problem in the solar neighborhood (van den Bergh 1962; Schmidt 1963; Sommer-Larsen 1991) and is also observed in other galaxies (e.g., Worthey et al. 1996). These observations strongly suggest the need for galaxy gas accretion.

However, direct observation of gas accretion onto galaxies remains sparse (Putman et al. 2012). Although the Milky Way (MW) is accreting gas (e.g., the Magel-

lanic Stream, Fox et al. 2014), our location in the MW makes it difficult to detect inflowing gas besides high velocity clouds (Zheng et al. 2015). Beyond the local universe, the detection rate of net inflow identified from galaxy spectra stays low at roughly 5% (Martin et al. 2012; Rubin et al. 2012). These down-the-barrel galaxy observations have been challenged by the fact that inflowing gas can be identified only if the Doppler shift can be distinguished from the velocity dispersion of the interstellar medium (ISM). Otherwise, the inflowing gas will produce absorption that overlaps with the dense ISM in wavelength (or velocity) space, and the true inflow mass flux will be underestimated.

In contrast to down-the-barrel observations, transverse sightlines through the circumgalactic medium (CGM, Tumlinson et al. 2017) eliminate the problem of overlapping absorption from the intervening CGM and the ISM. Transverse sightlines probe the CGM against bright background sources such as quasars. Recent quasar sightline studies use a series of metal absorption-line systems to provide better constraints on the significant cool ( $\sim 10^4\text{--}10^5 \text{ K}$ ) gas mass in the CGM. Together with the warm-hot phase, the CGM

potentially accounts for at least half and up to all of the missing baryons associated with galaxy halos (Werk et al. 2014; Prochaska et al. 2017, also see Stocke et al. 2013).

Recent measurements of circumgalactic absorption along quasar sightlines draw attention to the inhomogeneous distribution of baryons in the CGM. Sightlines along the galaxy major or minor axes frequently detect absorption systems with large equivalent widths and broad velocity ranges, but these strong absorbers are largely absent from sightlines that do not align with either of the two axes (Bouché et al. 2012; Kacprzak et al. 2012, 2015; Nielsen et al. 2015). This bi-modality in spatial geometry suggests the position of the sightline relative to the galactic disk potentially distinguishes the origin of the circumgalactic absorption.

Sightlines along galaxy major axes often detect circumgalactic absorption with the Doppler shift sharing the same sign as the galactic disk. This implies the CGM corotates with the galaxy disks out to large radii (Steidel et al. 2002; Kacprzak et al. 2010, 2011; Bouché et al. 2013, 2016; Diamond-Stanic et al. 2016; Ho et al. 2017; Martin et al. 2019). However, a simple rotating disk poorly reproduces the broad velocity ranges spanned by the absorption (Steidel et al. 2002; Kacprzak et al. 2010, 2011; Ho et al. 2017). Some studies even demonstrate that the corotation can be modeled as inflowing gas with a disk-like geometry (Bouché et al. 2016; Bowen et al. 2016; Ho et al. 2017). Hence, probing the CGM along galaxy major axes provides a promising strategy to explore how galaxies obtain their gas.

From the theoretical perspective, circumgalactic gas, especially for gas accreted in ‘cold-mode’, has significant angular momentum which can lead to corotation. In contrast to ‘hot-mode’, where shock-heated gas cools and accretes onto the central galaxies isotropically (Fall & Efstathiou 1980; Mo et al. 1998), ‘cold-mode’ gas has a cooling time shorter than the time needed to establish a stable shock (Dekel & Birnboim 2006; Kereš et al. 2005). Recent hydrodynamical simulations emphasize the importance of ‘cold-mode’ accretion. In addition to accreting along filamentary streams, cold-mode gas has higher specific angular momentum than its dark matter and ‘hot-mode’ gas counterparts (Kereš et al. 2009; Brook et al. 2011; Kimm et al. 2011; Stewart et al. 2011, 2013; Teklu et al. 2015; Stewart et al. 2017; Stevens et al. 2017).

In hydrodynamical simulations, galactic disks grow by accreting cooling, high angular momentum gas from the CGM. As gas streams fall toward a galaxy, torques generated by the disk align the infalling gas with the pre-existing disk (Danovich et al. 2012, 2015). The newly

accreted gas forms an extended cold flow disk, which corotates with the galaxy out to large radii (Stewart et al. 2011, 2013). With gas accreted at later times having higher specific angular momentum, galaxy disks thereby grow inside-out (Kimm et al. 2011; Pichon et al. 2011; Lagos et al. 2017; El-Badry et al. 2018).

This paper presents results from the EAGLE simulation suite (Schaye et al. 2015; Crain et al. 2015; McAlpine et al. 2016). EAGLE has been found to produce a realistic galaxy population and broadly reproduce a number of observations. These include the  $z \sim 0$  galaxy stellar mass function and the Tully-Fisher relation (Schaye et al. 2015), the evolution of galaxy masses (Furlong et al. 2015), the color bimodality of galaxies (Trayford et al. 2015, 2016), and the atomic (Bahé et al. 2016; Crain et al. 2017) and molecular gas (Lagos et al. 2015) content of galaxies. Similar to other hydrodynamical simulations that show cold gas with high specific angular momentum, Stevens et al. (2017) have demonstrated that both cooling gas and hot gas in EAGLE have higher specific angular momentum than the dark matter halo. Previous work using the EAGLE simulations (and OWLS, Schaye et al. 2010) has also demonstrated the importance of cold gas accretion onto galaxies (van de Voort et al. 2011; Correa et al. 2018a,b). Turner et al. (2017) have compared EAGLE mock spectra with metal-line absorption data of  $z \approx 2$  star-forming galaxies (Turner et al. 2014) in the Keck Baryonic Structure Survey (KBSS, Rudie et al. 2012; Steidel et al. 2014). The comparison has found evidence of infalling gas that explains the observed redshift-space distortions.

Using the EAGLE simulations, we examine how cold gas accretes onto galaxies and relate the gas kinematics to measurements in quasar sightline observations. We identify the inflowing gas particles using two methods: (i) the analytical ballistic approximation that predicts the motion of particles under the influence of gravity, and (ii) tracking particles through time in EAGLE which includes full hydrodynamic calculations. We study and compare the inflow properties from identifying inflow particles using the two methods, and we gain insight into the factors that affect whether a cold gas particle reaches the inner galaxy within a disk rotation period. To motivate the use of EAGLE simulations to explain the CGM observations in the future, we use mock sightlines to probe the cold gas around one of the EAGLE galaxies. We identify the structural features that can reproduce the corotation signature and the broad velocity ranges detected in quasar sightline observations. We defer the spectral analysis and the use of a large galaxy sample to a future paper.

We present the paper as follows. Section 2 describes the EAGLE galaxy selection at  $z = 0.27$ , and we demonstrate that the short gas consumption time demands an external gas supply. Then we identify the cold inflowing gas that feeds the inner galaxies and examine the inflow properties. We show the results of using the ballistic approximation and particle tracking in Section 3 and 4 respectively. In Section 5, we probe the cold gas around an EAGLE galaxy using mock quasar sightlines, and we focus on the gas structures that corotate with the disk and span broad velocity ranges. Finally, we summarize our results in Section 6.

## 2. GALAXY SELECTION FROM THE EAGLE SIMULATION

### 2.1. Simulation Overview

The EAGLE simulation suite consists of a large number of cosmological, hydrodynamic simulations (Schaye et al. 2015; Crain et al. 2015; McAlpine et al. 2016). EAGLE was run on a modified version of the  $N$ -Body Tree-PM smoothed particle hydrodynamics (SPH) code GADGET-3 (last described in Springel 2005). State-of-the-art subgrid models were implemented to capture unresolved physics, including radiative cooling and photoheating, star formation, stellar evolution and enrichment, stellar feedback, black hole growth, and feedback from active galactic nuclei. The simulations also varied in cosmological volumes, resolutions, and subgrid physics, and the stellar feedback was calibrated to reasonably reproduce sizes of disk galaxies, and the galaxy stellar mass function at  $z \sim 0$ .

EAGLE defines galaxies as gravitationally bound subhalos identified by the SUBFIND algorithm (Springel et al. 2001; Dolag et al. 2009). In brief, first the friends-of-friends (FoF) algorithm (Davis et al. 1985) places dark matter particles into the same group if the particle separation is below 0.2 times the average particle separation. Baryons are associated with the same FoF halo (if any) as their closest dark matter particle. Then, within FoF halos, SUBFIND defines self-bound overdensity substructures as subhalos, and each subhalo represents a galaxy. Within each FoF halo, the subhalo that contains the particle with the lowest value of gravitational potential is the central galaxy. The remaining subhalos are classified as satellite galaxies.

In this pilot study, we use the simulation Ref-L012N0188 with a box size of 12.5 cMpc. In the future, we will expand our study to large simulations and with higher resolutions. We summarize the simulation pa-

**Table 1.** Characteristics of the Ref-L012N0188 simulation used in this paper.

	Simulation Property	Value
(1)	Boxsize $L$ (cMpc)	12.5
(2)	Number of particles $N$	$188^3$
(3)	Initial baryonic particle mass $m_g$ ( $M_\odot$ )	$1.81 \times 10^6$
(4)	Dark matter particle mass $m_{\text{dm}}$ ( $M_\odot$ )	$9.70 \times 10^6$
(5)	Gravitational softening length $\epsilon_{\text{com}}$ (ckpc)	2.66
(6)	Maximum softening length $\epsilon_{\text{prop}}$ (pkpc)	0.70

NOTE— (1) Comoving boxsize. (2) Number of dark matter particles (initially there is an equal number of baryonic particles). (3) Initial baryonic particle mass. (4) Dark matter particle mass. (5) Comoving Plummer-equivalent gravitational softening length. (6) Maximum proper softening length.

rameters in Table 1. We use the particle data output<sup>1</sup> and mainly focus on galaxies at a single ‘snapshot’ of  $z = 0.271$ ; this redshift is comparable to the galaxy redshifts in quasar absorption line studies that measure the CGM kinematics of low redshift galaxies (e.g., Ho et al. 2017; Martin et al. 2019). In Section 4, we also show results from particle tracking at finer timesteps than consecutive snapshots; we use the reduced set of particle properties in ‘snapshots’.

### 2.2. Defining Cold Gas

In the simulation, we identify cold gas particles using temperature cutoffs. For most of this work, especially when we focus on cold inflowing gas (Section 3 and 4), we select cold gas using a temperature cutoff of  $2.5 \times 10^5$  K. This cutoff has been commonly used to distinguish between cold-mode and hot-mode accretion (Kereš et al. 2005, 2009; Stewart et al. 2013, 2017). However, when we compare cold gas kinematics to quasar sightline observations (Section 5), which detect absorption from low ionization ions (e.g., Mg II, Si II, Fe II), we redefine the cutoff as  $3 \times 10^4$  K. This is because low ions such as Mg II do not exist at  $\sim 10^5$  K (Oppenheimer & Schaye 2013; Tumlinson et al. 2017).

In addition, we assign all star-forming gas as ‘cold’ gas, because in EAGLE, the temperature of the star-forming (i.e., interstellar) gas is artificially increased to reflect the effective pressure. EAGLE lacks the resolution to resolve the interstellar gas phase of  $T_{\text{gas}} \ll 10^4$  K. Hence, EAGLE imposes a temperature floor, such that the corresponding effective equation of state prevents numerical Jeans fragmentation due to the finite resolution (Schaye

<sup>1</sup> Particle data from snapshots can be downloaded from <http://icc.dur.ac.uk/Eagle/database.php>

& Dalla Vecchia 2008, also see Robertson & Kravtsov 2008 and Schaye & Dalla Vecchia 2008).

### 2.3. Galaxy Selection

We select galaxies at  $z = 0.271$  with a stellar mass range of  $\log(M_*/M_\odot)$  between 9.5 and 10.5, comparable to that of the galaxy samples in Ho et al. (2017) and Martin et al. (2019) that study the CGM kinematics of low-redshift galaxies. To measure the stellar mass of each galaxy, we use a 3D aperture with a radius of 30 pkpc from the galaxy center<sup>2</sup>, and sum over the masses of star particles that belong to the subhalo (as defined in Schaye et al. 2015). Figure 1 shows the selected galaxies on the SFR– $M_*$  plane, for which we use the same 30-pkpc aperture to measure the SFR. We show the SFR– $M_*$  main sequence from Peng et al. (2010), fitted to the star-forming galaxies in the Sloan Digital Sky Survey (SDSS) from Brinchmann et al. (2004). We also plot the line that divides star-forming and quiescent galaxies (Moustakas et al. 2013); the line comes from a redshift dependent relation using  $\sim 120,000$  galaxies with spectroscopic redshifts from the PRISM Multi-object Survey (PRISM, Coil et al. 2011; Cool et al. 2013) and SDSS. Figure 1 shows that our selected galaxies lie along the main sequence. Star-forming galaxies dominate our sample, with most of them being central galaxies.

The halo virial masses of our sample range from  $\log(M_{\text{vir}}/M_\odot)$  of 11.5 to 12.6. We define the virial radius  $r_{\text{vir}}$  as the radius that encloses an average density of  $\Delta_{\text{vir}}(z)\rho_c(z)$ , where  $\rho_c(z)$  represents the critical density at redshift  $z$ , and the overdensity  $\Delta_{\text{vir}}(z)$  follows the top-hat spherical collapse calculation in Bryan & Norman (1998).<sup>3</sup>

### 2.4. Global Gas Consumption Timescale

The gas consumption timescale is sometimes referred as the ‘Roberts time’ (Roberts 1963), which is defined using the following relation (Kennicutt et al. 1994, hereafter K94),

$$\tau_R = \frac{M_{\text{gas}}/SFR}{1 - R} \quad (1)$$

where  $R$  is the returned gas fraction. The  $(1 - R)^{-1}$  correction factor accounts for gas recycling and future time dependence on SFR. K94 have analyzed how  $(1 - R)^{-1}$  changes with different parameters, such as initial mass functions, star formation laws, and gas surface density etc. From their time-dependent modeling of gas return

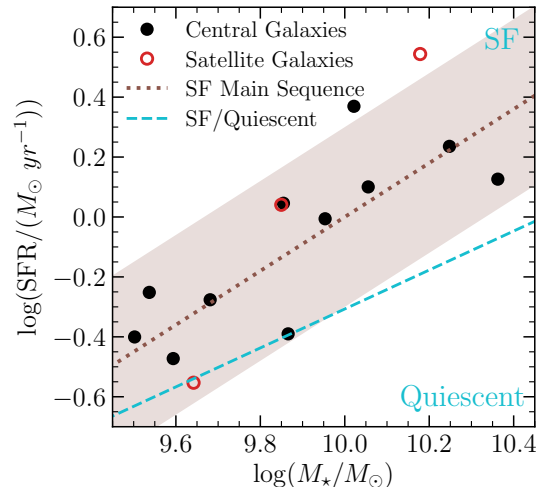


**Figure 1.** Galaxies on the SFR– $M_*$  plane. Black filled and red empty circles represent central and satellite galaxies, respectively. The brown dotted line and the shaded region show the star-forming main sequence and the 0.3 dex scatter from Peng et al. (2010), which fit the SDSS star-forming galaxies in Brinchmann et al. (2004). The cyan dashed line divides the sample into star-forming or quiescent, depending on whether the galaxies lie above or below the line (Moustakas et al. 2013). The selected galaxies lie along the main sequence, and most galaxies are star-forming.

rate (from stars), they suggest that recycling gas extends  $\tau_R$  of typical star-forming disks by 1.5 to 4 times.

For our selected EAGLE galaxies, we calculate the gas consumption time  $\tau_R$  using Equation (1). Including gas beyond the star-forming region will overestimate the actual gas depletion time in the inner galaxy regions, where star formation takes place. To avoid this overestimation, first we define the star-forming radius  $r_{\text{SFR}90}$  as the radius that encloses 90% of the galaxy SFR, and we round it up to the closest 5 pkpc<sup>4</sup>. Then, we calculate  $\tau_R$  using the gas mass and SFR within a 3D aperture of radius  $r_{\text{SFR}90}$ . In addition, we impose limits on gas temperature  $T_{\text{gas}}$  while calculating the gas mass: all  $T_{\text{gas}}$ ,  $T_{\text{gas}} \leq 2.5 \times 10^5$  K, and  $T_{\text{gas}} \leq 3 \times 10^4$  K.

Figure 2 shows the distribution of gas consumption time  $\tau_R$  of the galaxies. We show  $\tau_R$  before and after applying the  $(1 - R)^{-1}$  correction factor, i.e., set  $(1 - R)^{-1} = 1$  or use an assumed value of 2.5. The latter is consistent with K94,<sup>5</sup> and Figure 2 shows that their nearby galaxy sample (black histogram) and our selected galaxies have comparable gas consumption times. If

<sup>4</sup> We round up to the closest 1 pkpc, if the star-forming radius is below 5 pkpc.

<sup>5</sup>  $(1 - R)^{-1} = 2.5$  is also adopted in other publications, e.g., Boselli et al. (2001).

<sup>2</sup> The galaxy center is defined as the location of the most bound particle of the subhalo.

<sup>3</sup> At  $z = 0.271$ ,  $\Delta_{\text{vir}}(z) = 124$ .



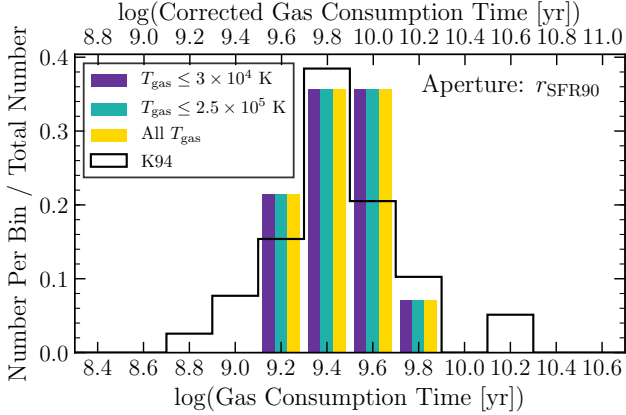


**Figure 2.** Distribution of gas consumption time. We calculate the gas consumption time using the gas mass and SFR within the star-forming radius  $r_{\text{SFR90}}$ . Within each histogram bin, different colors of the filled histograms distinguish the use of gas masses with different temperature limits. The bottom and top axis show the timescale before and after applying the gas recycling correction factor, i.e.,  $(1 - R)^{-1} = 1$  or 2.5. The black histogram shows the gas consumption time distribution of nearby galaxies in [Kennicutt et al. \(1994\)](#), and their calculation includes only the gas mass within the star-forming disk. Even with the  $(1 - R)^{-1}$  correction factor, at least half of the **EAGLE** galaxies have gas consumption timescales shorter than the Hubble time.

we adopt a fixed 30-pkpc aperture, i.e., the same aperture used to measure the stellar mass and SFR of a galaxy, then  $\tau_R$  of each galaxy increases by over 50% (0.2 dex). This is because star-forming regions are generally smaller than 30 pkpc, and hence a 30-pkpc aperture includes a larger gas reservoir without increasing the SFR. This phenomenon agrees with K94, who have also shown that including gas outside the star-forming radius increases  $\tau_R$ .

The gas consumption times of several Gyrs for our galaxies are also comparable to the atomic and molecular consumption timescales (uncorrected) of galaxies in other observed samples. For example, the nearby disk galaxies in the HERACLE survey have  $\text{H}_2$  consumption timescales of  $\sim 2.4$  Gyr ([Bigiel et al. 2008, 2011](#)), and the low-redshift,  $M_\star \sim 10^{10} M_\odot$  galaxies in the COLD GASS survey have  $\text{H I}$  and  $\text{H}_2$  consumption timescales of  $\sim 3$  Gyr and  $\sim 1$  Gyr respectively ([Schiminovich et al. 2010; Saintonge et al. 2011](#)); also see Section 4 of [Lagos et al. \(2015\)](#) for a detailed comparison of  $\text{H}_2$  consumption timescales between **EAGLE** and COLD GASS galaxies.

Furthermore, while Figure 2 shows that  $\tau_R$  of the **EAGLE** galaxies do not vary significantly with the temperature cuts,  $\tau_R$  shows a stronger temperature dependence if we adopt a fixed 30-pkpc aperture. This suggests cold

gas with temperature below  $3 \times 10^4$  K dominates the total gas mass within  $r_{\text{SFR90}}$ .

Regardless of our gas temperature limit, and even if we apply the  $(1 - R)^{-1}$  correction factor, Figure 2 shows that gas consumption timescales of at least half of the galaxies are significantly shorter than the Hubble time. This implies that in order to sustain the star-forming activity, the galaxies have to replenish their gas supply.

### 3. IDENTIFICATION OF INFLOWING COLD GAS

We aim to understand how galaxies get the gas to fuel star formation. Hot, virialized gas does not directly accrete onto galaxies. Even in the hot-mode accretion scenario, the virialized gas has to cool and condense, before being accreted to form stars. In the cold-mode scenario, the accreted gas remains cold during accretion. Therefore, we focus on the accretion of cold gas onto galaxies. In Section 4, by identifying inflowing gas through tracking particles, we will verify that, at least for our selected central galaxies in **EAGLE**, inflow from hot gas is negligible. That will justify our focus on considering cold gas only in this section.

We want to identify the cold gas particles that will fall into the galactic disk within a rotation period. In principle, we can do so by tracking particles through time. However, the simulation only produces snapshot output at coarse redshift (i.e., time) intervals typically larger than a rotation period. And in general, tracking the particle positions at finer timesteps than the default simulation output requires re-running the simulation, which may be impossible if one only has access to output at preset time intervals. Running future cosmological simulations will also become more computationally expensive, making it hard or even impossible to save the full simulation output at fine timesteps. As a result, the reconstruction of gas infall rates by tracking particles through time will be difficult. Therefore, in this section, we introduce a procedure to estimate the infall from the simulation output at a single time step.

We neglect pressure forces on the cold gas and calculate the orbits of gas particles in the gravitational potential. Orbits that reach pericenter beyond the galactic disk cannot feed the disk. We are interested in the orbits that intersect the galactic disk, because the collision of the cloud with the gas disk or the dense star-forming region will dissipate energy. We assume such gas will be incorporated into the disk as fuel. We then estimate a mean accretion rate and the average inflow speed over a disk rotation period. We also examine the distribution of the inflowing gas and its angular momentum. Then in Section 4, we will discuss the validity and the caveats of this simple, analytical calculation of the bal-

ballistic approximation, and we will explore whether the ballistic approximation can reasonably reproduce the inflow properties. For the analysis in this Section and Section 4, we will only focus on the central galaxies and exclude the satellite galaxies.

### 3.1. Ballistic Approximation

To identify the inflowing cold gas ( $T_{\text{gas}} \leq 2.5 \times 10^5$  K), we predict whether individual cold gas particles can reach the star-forming region within a rotation period. We define the star-forming region as a spherical region of radius  $r_{\text{SFR90}}$  (defined in Section 2.4) from the galaxy center. We set the rotation period as  $4 \times \sqrt{3\pi/(16G\langle\rho\rangle)}$ , where  $\langle\rho\rangle$  represents the average density of the star-forming region. We calculate each particle orbit within a rotation period of the star-forming region. Each particle conserves energy and angular momentum, and the particle moves in a centrally directed gravitational field characterized by the dark matter. In the absence of hydrodynamical interactions between particles, the gravitational force determines the particle trajectory. Hence, we characterize the radial motion of each particle by

$$\ddot{r} = f_{\text{grav}}(r) + \frac{j^2}{r^3}, \quad (2)$$

$$\varepsilon = \frac{1}{2}\dot{r}^2 + \frac{j^2}{2r^2} + \Phi_{\text{grav}}(r), \quad (3)$$

where  $f_{\text{grav}}(r) = -\partial\Phi_{\text{grav}}(r)/\partial r$  represents the gravitational force per unit mass at radius  $r$ , and  $j$  and  $\varepsilon$  represent the constant specific angular momentum and energy of the particle. If the particle orbit ever intersects the star-forming region, then we consider the particle as inflowing.

We justify our assumption of gravitational force dominating over the pressure force on the cold gas as follows. Analogous to a multi-phase interstellar medium (ISM) model, gas of different phases, e.g., cold ( $\sim 10^4$  K) and hot ( $\sim 10^6$  K) gas, reach pressure equilibrium and thereby share a similar pressure gradient, i.e.,  $\nabla P_{\text{cold}} \approx \nabla P_{\text{hot}}$ . The cold gas has a higher density, i.e.,  $\rho_{\text{cold}} \gg \rho_{\text{hot}}$ , since gas density scales inversely with temperature. As a result, the cold gas experiences a smaller pressure force because  $|\nabla P_{\text{cold}}/\rho_{\text{cold}}| \ll |\nabla P_{\text{hot}}/\rho_{\text{hot}}|$ . For the virialized hot gas, the pressure force balances the gravitational pull and prevents the gas from collapsing by its own gravity. Since the cold gas experiences a smaller pressure force than the hot gas, the pressure force on the cold gas is negligible compared to gravity. Hence, for the cold gas, the gravitational force dominates.

We expect the ballistic approximation to break down under the following circumstances. First, if the cold gas clouds intercept hot gas with comparable mass column density, then the cold gas will be suspended by

the hot gas, which prevents the cold clouds from falling in. Because this scenario violates the assumption of the ballistic approximation that the gravitational force dominates over the pressure force, the ballistic approximation becomes invalid. Second, although we assume any gas that reaches the star-forming region will be incorporated into the disk, this neglects the presence of galactic winds. Not only can winds remove gas that has once accreted onto the star-forming disk, they can also push out gas that would otherwise be accreted. Consequently, whether the gas remains in the disk as fuel is sensitive to feedback, which the ballistic approximation ignores. Third, gas particles may lose angular momentum due to the interactions and collisions between them, e.g., with other cold infalling gas particles or with the pre-existing disk (Danovich et al. 2015; Stevens et al. 2017)<sup>6</sup>. The angular momentum dissipation thereby depends on the distribution of the gas particles and the frequency of particle collision, which the ballistic approximation neglects. Keeping these caveats in mind, we will identify the inflowing gas and predict the inflow properties using this analytical calculation. Section 4 will explore the validity of the ballistic approximation. We will show that although the ballistic approximation can estimate the mass inflow rate to within a factor of two compared to that from particle tracking, the prediction is less accurate for the average radial inflow speed. Our analysis will thereby suggest that generally, the reconstruction of gas inflow properties, including inflow rates and inflow speeds, will benefit from simulation output at higher time cadence, e.g., at the order of the rotation timescale of  $\sim 100$  Myr.

### 3.2. Geometry of the Inflowing Cold Gas

In this section, we examine the distribution and the morphological structure of the inflowing cold gas. As an example, we show a galaxy (ID: 37448) in Figure 3, and we project the cold gas particles ( $T_{\text{gas}} \leq 2.5 \times 10^5$  K) onto 2D planes. First, panels (a) to (c) indicate that the galaxy has a rotating structure. The blueshifted and redshifted particle projected velocities clearly show that the galaxy has an approaching and a receding side. Second, panel (a) also illustrates that most particles reside in a thin structure, and the galaxy resembles a disk morphology. To visualize the distribution of the inflowing gas, in panels (d) to (f), the colors of the gas particles show whether the particles will reach the star-forming

<sup>6</sup> Specifically, Stevens et al. (2017) use **EAGLE** and study the change of angular momentum of the *cooling* gas, i.e., gas that transitioned from hot to cold phase, and find non-negligible angular momentum loss.

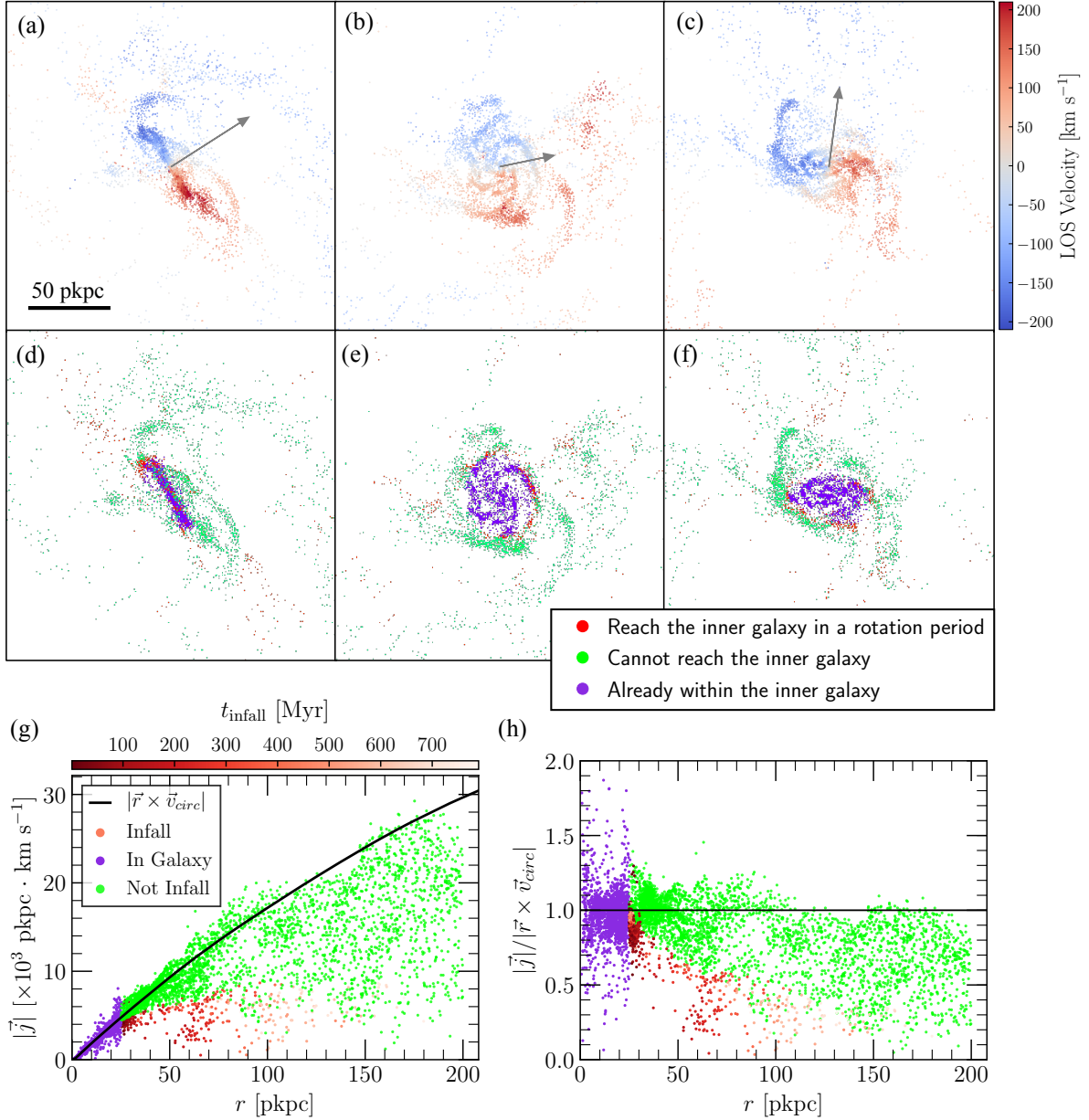


**Figure 3.** Cold gas with  $T_{\text{gas}} \leq 2.5 \times 10^5$  K of a disk galaxy (galaxy ID: 37448). The top two rows (panels a to f) show the projection plots of cold gas particles, and each column shows a cut in  $x$ ,  $y$  and  $z$  plane respectively. Each panel is  $200 \text{ pkpc} \times 200 \text{ pkpc}$ . (*Top row, panels a to c*) Particles are color-coded by their projected LOS velocities, which clearly show a disk-like rotating structure. The gray arrows show the direction of the net angular momentum (projected onto each 2D plane) of the inner cold gas disk. The galaxy has an approaching (blueshifted) and a receding (redshifted) side, which indicates the presence of a rotating structure. (*Middle row, panels d to f*) Particles are color-coded by whether they will reach the star-forming region in our ballistic approximation. Most inflowing gas particles (red) reside at the outer spiral arms. (*Bottom row, panels g and h*) The left panel shows the specific angular momentum  $|\vec{j}|$  of each particle. The black line shows the specific angular momentum required for the particle to be rotationally supported, i.e.,  $|\vec{r} \times \vec{v}_{\text{circ}}|$ , where  $\vec{v}_{\text{circ}}$  is the circular velocity at radius  $r$ . The right panel normalizes each particle  $|\vec{j}|$  by  $|\vec{r} \times \vec{v}_{\text{circ}}|$ . Most infalling gas particles lack sufficient angular momentum to maintain circular orbits, since  $|\vec{j}|/|\vec{r} \times \vec{v}_{\text{circ}}| < 1$  for most infalling particles.

region, i.e., inflowing. Most inflowing gas particles (red dots) reside in the outer spiral arms.

Analogous to Figure 3, Figure 4 shows the remaining 10 central galaxies, and we use the same color scheme as in Figures 3(d) to (f) to distinguish the inflowing particles. A similar figure with particles color-coded by the particle projected velocities can be found at the Appendix. The particle projection plots in Figure 3 and 4 (and the Appendix) show that despite the different morphologies among galaxies, most galaxies have rotating structures. The infalling gas particles are distributed anisotropically and form a variety of structures, e.g., particles are concentrated along streams or are located near the thin, ‘disk-like’ structures as in Figure 3.

To quantify the spatial distribution of inflowing gas particles, we calculate their positions relative to the plane of the cold gas disk. For each galaxy, we define disk plane using the net angular momentum vector of cold gas. We allow the disk plane to change with radius, since H I observations often find warped gas disks (e.g., Heald et al. 2011; Zschaechner et al. 2012), and we measure the net angular momentum vector in concentric shells with thickness of  $\Delta r = 10$  pkpc. Figure 5 shows the cumulative mass profiles of the inflowing gas relative to the warped disk planes. The thin, cyan lines represent individual galaxies, and the thick, orange solid and dashed lines represent the median and the 68% confident levels of the sample. The profiles show that the inflowing particles extend further in the  $R$ -direction on the disk plane than in the  $|Z|$ -direction perpendicular to the disk plane. As an illustration, the black dotted lines show that from the median profiles,  $R \approx 0.35r_{\text{vir}}$  encloses 90% of the inflowing gas mass, in contrast to  $0.2r_{\text{vir}}$  in the  $|Z|$ -direction. On the one hand,  $0.2r_{\text{vir}}$  or tens of pkpc (Table 2 shows  $r_{\text{vir}}$  of each galaxy) along the  $|Z|$ -direction implies that the infalling particles do not just lie on a thin disk. But on the other hand, as the inflowing gas particles extend further in the  $R$ -direction than in the  $|Z|$ -direction, the gas tends to have a cylindrical structure, instead of an isotropic distribution.

### 3.3. Angular Momentum of Inflowing Gas

Figures 3(g) and (h) show the specific angular momentum  $|\vec{j}|$  of each cold gas particle. To be rotationally supported, each particle requires a specific angular momentum of  $|\vec{j}_{\text{circ}}| = |\vec{r} \times \vec{v}_{\text{circ}}|$  (solid line), where  $\vec{v}_{\text{circ}}$  is the circular velocity at radius  $r$ . Except for the inflowing gas at  $r \approx r_{\text{SFR90}}$ , most inflowing particles have  $|\vec{j}|/|\vec{j}_{\text{circ}}| < 1$ . Thus, these particles lack sufficient angular momentum to be on circular orbits. Inflowing gas of other central galaxies also show the same characteristics.

Without angular momentum, a particle will fall radially towards the galaxy center due to the gravity. Angular momentum provides rotational support for a particle. Under the assumption of angular momentum conservation, the particle  $|\vec{j}|$  defines the pericenter of the particle orbit, and only particles with pericenters smaller than the star-forming radius  $r_{\text{SFR90}}$  can possibly be considered as inflowing. In reality, however, a particle may lose angular momentum due to tidal interactions with the existing disk. Hence, the predicted pericenter represents an upper limit, and more particles than predicted may reach  $r_{\text{SFR90}}$  within a rotation period.

### 3.4. Average Mass Inflow Rate and SFR

Unless galaxies replenish their gas, galaxies will eventually quench due to the lack of fuel. The inflow rate provides an important clue of whether a galaxy can sustain its star formation rate. To calculate the average mass inflow rate  $\dot{M}_{\text{in}}^{\text{ballistic}}$ , we sum over the mass of the inflowing cold gas and divide it by the rotation period of each galaxy. We list  $\dot{M}_{\text{in}}^{\text{ballistic}}$  for individual galaxies in Table 2. Figure 6 compares  $\dot{M}_{\text{in}}^{\text{ballistic}}$  to the galaxy SFR (blue circles), and the figure shows that  $\dot{M}_{\text{in}}^{\text{ballistic}}$  exceeds the SFR for all central galaxies.

Equality between the average mass inflow rate and the galaxy SFR does not imply a sustainable star formation rate. Gas outflows remove gas from the galaxy and thereby demand a higher inflow rate to support star formation, whereas the recycling stellar gas reduces the need for new gas supply. In a self-sustainable evolution model, i.e., equilibrium model, a galaxy reaches equilibrium when the gas inflow rate is equal to a linear combination of the SFR and the gas outflow rate (Bouché et al. 2010; Davé et al. 2012). Under the equilibrium condition, we express the inflow rate  $\dot{M}_{\text{gas,in}}$  as

$$\dot{M}_{\text{gas,in}} = (1 - R)\dot{M}_{\star} + \dot{M}_{\text{gas,out}}, \quad (4)$$

where  $\dot{M}_{\text{gas,out}}$  and  $\dot{M}_{\star}$  represent the mass outflow rate and SFR respectively. The  $(1 - R)$  factor corrects for the gas recycling fraction, and hence  $(1 - R)\dot{M}_{\star}$  represents the corrected net SFR. The mass outflow rate scales with the SFR according to the mass loading factor,  $\eta = \dot{M}_{\text{gas,out}}/\text{SFR}$ . For simplicity, we use  $R = 0.52$  as in Bouché et al. (2010)<sup>7</sup>. While  $\eta$  is not well-constrained in observations due to the uncertainties in mass outflow rates, we adopt  $\eta \sim 1$  and 2 (dotted and dot-dashed lines respectively in Figure 6), typically inferred from observations for galaxies with similar stellar masses as our EAGLE galaxies (Martin et al. 2012; Kacprzak et al.

<sup>7</sup> Adopting  $R = 0.6$  as in Section 2.4 will have a negligible effect on the equilibrium expectation in Figure 6.



**Table 2.** Mass inflow rate and mass-weighted average inflow speed of cold gas ( $T_{\text{gas}} \leq 2.5 \times 10^5$  K) at central galaxies

Galaxy ID	$\log(M_*/M_\odot)$	$r_{\text{vir}}$	SFR	$\dot{M}_{\text{in}}^{\text{ballistic}}$	$\langle v_r \rangle_{\text{in}}^{\text{ballistic}}$	$\langle v_r \rangle_{\text{in,top10\%}}^{\text{ballistic}}$	$\dot{M}_{\text{in}}^{\text{tracking}}$	$\langle v_r \rangle_{\text{in}}^{\text{tracking}}$	$\langle v_r \rangle_{\text{in,top10\%}}^{\text{tracking}}$
		(kpc)	( $M_\odot \text{ yr}^{-1}$ )	( $M_\odot \text{ yr}^{-1}$ )	( $\text{km s}^{-1}$ )	( $\text{km s}^{-1}$ )	( $M_\odot \text{ yr}^{-1}$ )	( $\text{km s}^{-1}$ )	( $\text{km s}^{-1}$ )
(1)	(2)	(3)	(4)	(5)	(6)	(7)	(8)	(9)	(10)
37448	10.36	238	1.34	1.49	34	132	0.982	17	67
43166	10.25	197	1.72	2.23	62	161	1.67	42	164
32523	10.06	190	1.26	2.12	37	123	1.14	34	103
30497	10.02	219	2.34	11.5	61	206	6.57	48	140
40127	9.95	227	0.99	6.00	35	143	3.29	39	117
48386	9.87	186	0.41	0.863	30	100	0.0380	20	26
44548	9.85	185	1.11	4.14	40	155	2.89	40	148
57650	9.68	156	0.53	2.75	36	117	1.10	18	55
46369	9.59	177	0.34	1.85	45	102	1.08	59	99
51643	9.54	168	0.56	1.74	39	128	1.63	22	61
53907	9.50	166	0.40	1.73	17	49	1.15	25	57

NOTE— (1) Galaxy ID. (2) Stellar mass. (3) Virial radius. (4) Star formation rate. (5) Average mass inflow rate from inflow particles in the ballistic calculation. (6) Mass-weighted average inflow speed from inflow particles in the ballistic calculation. (7) Mass-weighted average inflow speed (10% mass with highest inflow speeds) from inflow particles in the ballistic calculation. (8) Average mass inflow rate from tracking inflow particles. (9) Mass-weighted average inflow speed from tracking inflow particles. (10) Mass-weighted average inflow speed (10% mass with highest inflow speeds) from tracking inflow particles.

2014; Heckman et al. 2015), as well as dwarf galaxies (Martin 1999) and infrared-luminous galaxies (Rupke et al. 2005). Figure 6 shows that the inflow rates are comparable to that expected by the equilibrium models, suggesting that the cold inflowing gas plausibly accounts for sustaining the galaxy star formation activities. We further discuss the comparison between inflow rates and SFRs and the implication in Section 4.2.

### 3.5. Mass-weighted Average Inflow Speed

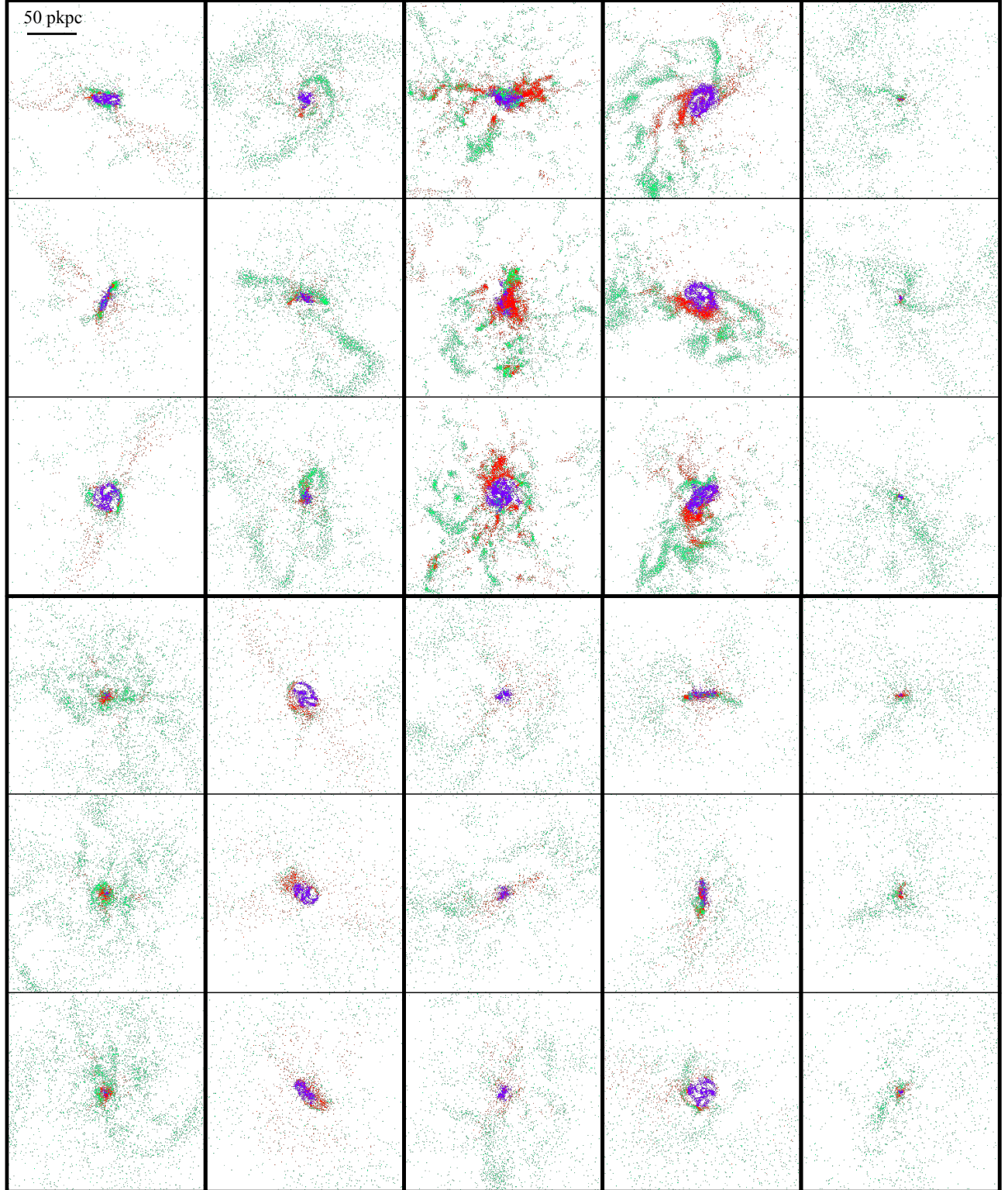
To estimate the average inflow speed over the rotation period, we take the mass-weighted average of the inflow speeds of individual inflowing cold gas particles. First, for each inflowing cold gas particle, we calculate its inflow speed from the change in radial distance from the galaxy center,  $\Delta r$ , and divide it by the rotation period. However, the ballistic approximation breaks down when the particle enters the star-forming region. Once the gas particle collides with the dense gas clouds in the star-forming region and dissipates energy, our assumption of energy conservation no longer holds. Therefore, we estimate  $\Delta r$  by differencing the initial particle radial position and the star-forming radius  $r_{\text{SFR90}}$ ; we assume the particle halts once it reaches  $r_{\text{SFR90}}$ . Then, we weight the inflow speeds of all inflowing gas particles by their particle masses, and we obtain the mass-weighted average inflow speed  $\langle v_r \rangle_{\text{in}}^{\text{ballistic}}$  for each galaxy.

Table 2 lists the mass-weighted average inflow speed  $\langle v_r \rangle_{\text{in}}^{\text{ballistic}}$  for the central galaxies, which ranges from  $17 \text{ km s}^{-1}$  to  $62 \text{ km s}^{-1}$ . Although most particles have

low inflow speeds, resulting in low  $\langle v_r \rangle_{\text{in}}^{\text{ballistic}}$ , the particle inflow speeds often span a large range, and the distribution has a high velocity tail. To characterize the spread in individual inflow speeds, we also estimate the mass-weighted average inflow speed using the subset of particles with the highest inflow speeds; this particle subset accounts for 10% of the total inflowing gas mass. We show this average inflow speed from the ‘high speed tail’ as  $\langle v_r \rangle_{\text{in,top10\%}}^{\text{ballistic}}$  in Table 2. For most galaxies,  $\langle v_r \rangle_{\text{in,top10\%}}^{\text{ballistic}}$  exceeds  $100 \text{ km s}^{-1}$ . The significant difference between  $\langle v_r \rangle_{\text{in}}^{\text{ballistic}}$  and  $\langle v_r \rangle_{\text{in,top10\%}}^{\text{ballistic}}$  demonstrates the large spread in particle inflow speeds despite the low mass-weighted average.

## 4. BALLISTIC APPROXIMATION VS. HYDRODYNAMIC CALCULATIONS

Instead of tracking particles through continuous time, the ballistic approximation provides an alternate method to predict the properties of gas inflows. To understand how the gas inflow properties from the ballistic approximation compare to that from the hydrodynamic calculations in EAGLE, we track the gas particles through ‘snippets’. Snippets are output from the same EAGLE run, sampled at finer time intervals but with less information per particle compared to the full ‘snapshot’ output. This allows us to select the time slice around the rotation period of a galaxy. In Section 4.1, we explain how we track particles to define inflowing cold gas. Section 4.2 compares the average mass inflow rate



**Figure 4.** Particle projection plots showing whether the cold gas particles can reach the star-forming region within a rotation period. The particles have the same color-coding as in panel (d) to (f) of Figure 3. Each galaxy occupies 3 rows  $\times$  1 column, enclosed by the thick black lines. For individual galaxies, from top to bottom, each panel represents the cut in  $x$ ,  $y$  and  $z$  plane respectively, and has a side length of 200 pkpc. The plotted central galaxies are ordered in decreasing stellar masses, from left to right, and top to bottom.

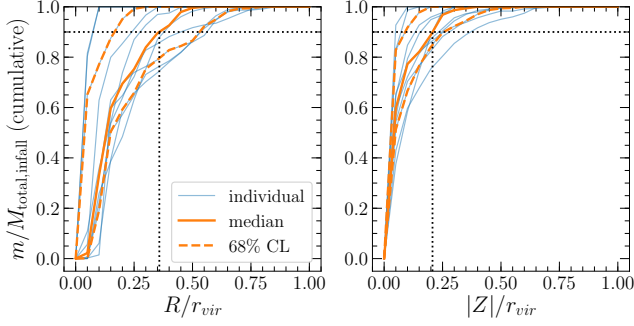


**Figure 5.** Spatial distribution of cold inflowing gas particles relative to warped disk planes. The left and the right panels show the cumulative mass profiles of the inflowing gas in radial  $R$ , and perpendicular  $|Z|$  direction relative to the disk planes respectively (i.e., in cylindrical coordinates). Both  $R$  and  $|Z|$  are normalized by the galaxy virial radius  $r_{\text{vir}}$ , and the mass profiles are normalized by the total mass of the infalling gas. Thin, cyan lines represent individual central galaxies, and the thick, orange solid and dashed lines show the median and the 68% confidence level. As measured from the median profiles, enclosing 90% of the inflowing gas mass requires  $R \approx 0.35r_{\text{vir}}$  and  $|Z| \approx 0.2r_{\text{vir}}$  (black dotted lines). The inflowing gas particles extend further in the  $R$ -direction compared to the  $|Z|$ -direction.

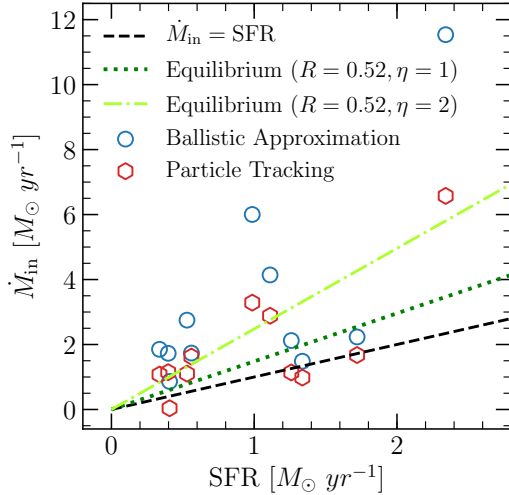


**Figure 6.** Comparison between average mass inflow rates and SFRs of central galaxies. The ballistic approximation (blue circles) generally overestimates the cold gas inflow rate compared to particle tracking (red hexagons). The inflow rates are comparable to that suggested by the equilibrium model; we show the case for  $R = 0.52$  and  $\eta = 1$  (dotted) and  $\eta = 2$  (dot-dashed) in Equation 4. The cold gas inflow plausibly accounts for sustaining the galaxy star formation activities.

obtained from both the ballistic approximation and particle tracking, whereas Section 4.3 compares the mass-weighted average inflow speed using the two methods.

In Section 4.4, we explore how the newly accreted gas contributes to recent star formation. Section 4.5 discusses the limitations of the ballistic approximation and the caveats of comparing its inflow prediction to the outcome of EAGLE’s hydrodynamical calculations.

#### 4.1. Tracking Gas Particles to Identify Inflowing Gas

We follow each gas particle through EAGLE snapshots, sampled at every  $\sim 70$  Myr around  $z \sim 0.271$ . To identify the inflowing cold gas particles for each galaxy, first we choose the snapshot for which the time evolved from  $z = 0.271$  is closest to the galaxy rotation period. Hence, we use different snapshots for different galaxies. We define cold gas using the same criteria in Section 2.2. To classify a gas particle as inflowing, the particle has to reside beyond  $r_{\text{SFR}90}$  at  $z = 0.271$  and have reached  $r_{\text{SFR}90}(z = 0.271)$  or deeper after the rotation period in the selected snapshots. If this particle has been converted into a star, we still classify it as an inflowing gas particle. Since only a tiny fraction of inflowing gas particles have turned into stars after a rotation period, our conclusions will not change even if we exclude this inflowing particle subset.

In our ballistic approximation, we have assumed that inflow from hot gas is negligible and only focused on cold gas with  $T_{\text{gas}} \leq 2.5 \times 10^5$  K. Figure 7 justifies this assumption. Through particle tracking, comparing the inflow mass with and without applying a temperature cutoff  $T_{\text{gas}}(z = 0.271)$  (red hexagons and gray diamonds) shows that over 95% of the tracked inflowing gas (by mass) is cold. This implies that for our selected EAGLE galaxies, inflow from cold gas dominates.

Using the results of particle tracking and the prediction of the ballistic approximation, Figure 7 compares the inflowing gas mass from both methods. The inflow mass from the ballistic approximation generally exceeds the traced inflow mass by a factor of 1.5 to 2 (blue circles). To understand what contributes to this factor of two overestimation, we sub-divide the gas particles into three categories: (I) predicted cold inflow from the ballistic approximation, and the particles have reached  $r_{\text{SFR}90}$  (green triangles), (II) predicted cold inflow from the ballistic approximation, but the particles still reside outside of  $r_{\text{SFR}90}$  (orange squares), and (III) not predicted as cold inflow, but the particles have reached  $r_{\text{SFR}90}$  (inverted brown triangles). While over 50% of the predicted inflowing gas really reaches the star-forming region (type I), a significant fraction of the predicted inflow fails to be accreted (type II). In contrast, the amount of unpredicted inflowing gas (type III) stays relatively low. Therefore, the factor of two difference in inflowing mass comes from the correct in-

flow prediction, as well as the compensation between the unpredicted inflow and the particles incorrectly predicted as inflow. As we will discuss in Section 4.5, this discrepancy is mainly caused by feedback.

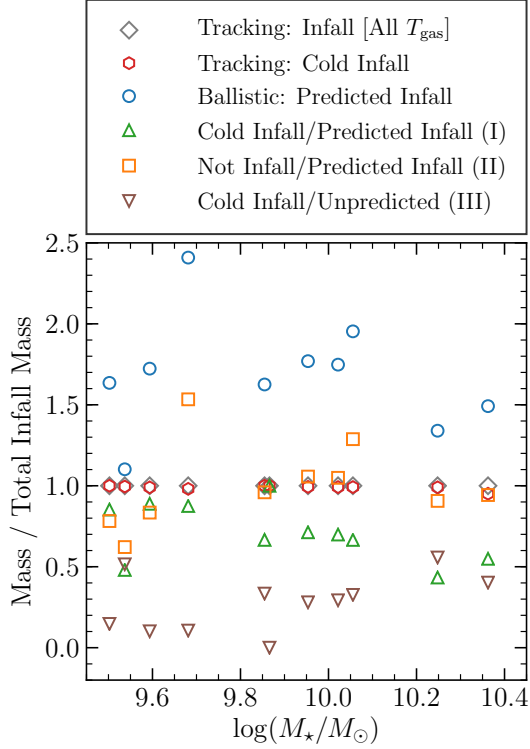


**Figure 7.** Comparison of inflowing gas mass between ballistic approximation and particle tracking. The masses of inflowing gas of different subsets (see legend) are normalized by the total mass of inflowing gas at all temperatures. Compared to the ‘true’ inflow mass that has reached the star-forming region, our ballistic approximation generally overestimates the inflowing mass by a factor of 1.5 to 2. See Section 4.2 for details.

#### 4.2. Average Mass Inflow Rate from Particle Tracking

We calculate the average mass inflow rate by summing the masses of identified inflow gas particles and dividing it by the time evolved from  $z = 0.271$  to the selected snapshot. Table 2 lists the inflow rate in column  $\dot{M}_{\text{in}}^{\text{tracking}}$ .

Figure 8 shows the tracked inflow rate from cold gas particles, and we compare that with the tracked inflow rate from gas at all temperatures and the predicted inflow rate from the ballistic approximation. The tracked inflow rate from cold gas matches that from gas at all temperatures. This suggests that most inflowing gas is cold (as deduced from Figure 7). Figure 8 also shows that the predicted inflow rates from the ballistic approx-

imation correlate with the tracked inflow rates. All predicted inflow rates exceed the tracked inflow rates, however, and with the exception of two galaxies, the overestimations are within a factor of two. For the galaxy that shows the largest discrepancy (ID: 48386), feedback has removed most of the gas from the star-forming region, resulting in a low average inflow rate. We will discuss how feedback affects the average mass inflow rate in Section 4.5.

We also compare the tracked inflow rates to the galaxy SFRs in Figure 6 (red hexagons). Although the inflow rates from particle tracking are lower than those from the ballistic approximation, Figure 6 still shows that most galaxies have comparable inflow rates and SFRs. This suggests that even without other types of inflows, such as satellite accretion and hot gas accretion (negligible as deduced in Figure 7), the cold gas inflow alone can account for most of the fuel needed to sustain the star formation in galaxies.

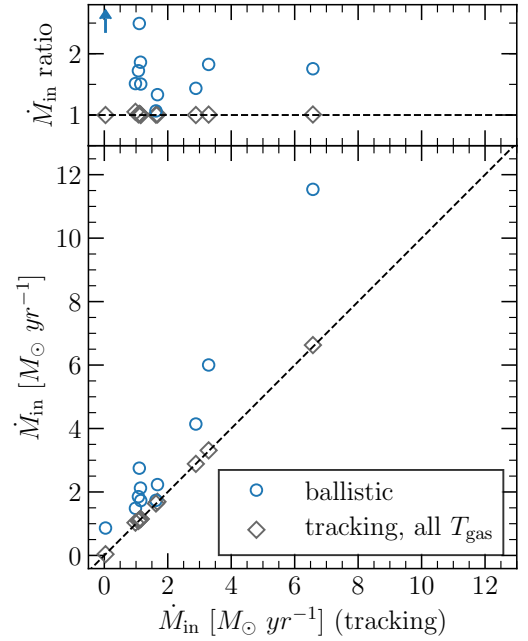


**Figure 8.** Average mass inflow rate from ballistic approximation and particle tracking. The horizontal axis shows the tracked inflow rate from cold gas ( $T_{\text{gas}} \leq 2.5 \times 10^5$  K) of the 11 central galaxies. The cyan circles show the predicted inflow rates from cold gas using the ballistic approximation, and the gray diamonds show the tracked inflow rates from gas at all temperatures. The top panel shows the ratio between each of these quantities and the tracked inflow rate from cold gas. The up arrow indicates that the value exceeds the axis limit.



#### 4.3. Mass-weighted Average Inflow Speed from Particle Tracking

We calculate the average inflow speed as in Section 3.5, but with two differences. First, instead of assuming the inflowing gas particles halt at  $r_{\text{SFR}90}$ , we calculate  $\Delta r$  as the change in radial distance relative to the galaxy center. Second, we divide  $\Delta r$  by the time evolved from  $z = 0.271$  to the selected snapshot, instead of the galaxy rotation period. In Table 2,  $\langle v_r \rangle_{\text{in}}^{\text{tracking}}$  shows the mass-weighted average inflow speed, and  $\langle v_r \rangle_{\text{in, top10\%}}^{\text{tracking}}$  shows the mass-weighted average from only the 10% particles by mass that have the highest inflow speeds. Figure 9 shows these two sets of average inflow speeds calculated from the cold gas, and compare them with the predicted inflow speeds from the ballistic approximation.

The average inflow speeds calculated from particle tracking share similar characteristics as those from the ballistic approximation: (1) low mass-weighted average inflow speed of  $\lesssim 60 \text{ km s}^{-1}$ , (2) large range of individual particle inflow speeds with a ‘high speed tail’, and (3) if we only consider 10% of the particles by mass with the highest individual inflow speeds, then the mass-weighted average ( $\langle v_r \rangle_{\text{in, top10\%}}^{\text{tracking}}$ ) often exceeds  $100 \text{ km s}^{-1}$ . In addition, for both sets of average inflow speeds, i.e., either from all cold gas or only cold gas particles at the high end of inflow speeds, the ballistic approximation overestimates the average inflow speeds for most galaxies. The differences in inflow speeds from the ballistic approximation and particle tracking mostly stay within a factor of two. The only exception is the galaxy (ID: 48386) with feedback removing most of the gas from the star-forming region (see Section 4.2 and 4.5).

However, unlike the mass inflow rate that shows a correlation between the prediction from the ballistic approximation and the calculation from particle tracking, inflow speeds do not reveal the same characteristic. While one possible explanation is the mismatch of inflowing particles identified by the two methods, another reason is due to the assumption of the ballistic approximation. When we calculate the average radial inflow speed for the ballistic approximation, because the approximation breaks down when a particle interacts with the dense clouds in the star-forming region, we assume the particle halts when it reaches the star-forming region. However, in reality, where the particle ends up depends on the density and the distribution of cold gas within the star-forming region, both of which the ballistic approximation ignores. Therefore, even though the average radial inflow speeds from ballistic approximation and particle tracking agree within a factor of two, the lack of correlation suggests the ballistic approximation does not provide a satisfactory estimate on the in-

flow speed. Hence, this suggests that inflow speed estimation, and generally, inflow properties reconstruction, require tracking particles at series of simulation output with higher time candence, preferably of the order of  $\sim 100 \text{ Myr}$ , i.e., around (or shorter than) the rotation period of a galaxy.

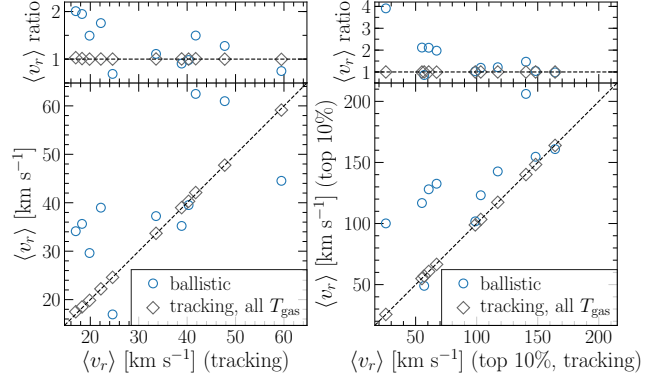


**Figure 9.** Mass-weighted average inflow speed from ballistic approximation and particle tracking. The left panel shows the mass-weighted average inflow speed, and the right panel shows the mass-weighted average calculated from 10% of the particles by mass that have the highest particle inflow speeds. Each horizontal axis shows the average inflow speed of the cold gas ( $T_{\text{gas}} \leq 2.5 \times 10^5 \text{ K}$ ) in particle tracking. The cyan circles show the mass-weighted average from cold inflowing gas using the ballistic approximation, and the gray diamonds show the mass-weighted average of the tracked inflow gas at all temperatures. The top panels show the ratio between each of these quantities to the mass-weighted average inflow speed of the tracked cold gas (i.e., the quantity plotted on the horizontal axis).

#### 4.4. Star Formation from Gas Accreted onto the Inner Galaxy

Gas accreted onto galaxies eventually forms stars. For each galaxy, we identify the gas at  $z = 0.271$  that has turned into stars at the selected snapshot after a rotation period. Although most of these particles reside within  $r_{\text{SFR}90}(z = 0.271)$  at both times, on average, around 10% of the new stars are formed from the newly accreted gas that originally resided outside of  $r_{\text{SFR}90}$ .

Figure 10 shows two galaxy examples, and the red points illustrate the gas particles that have turned into stars after a rotation period. Most of these particles originally resided along the spiral arms. After a rotation period, these particles become more concentrated near each galaxy center, where some of these particles are newly accreted from outside of  $r_{\text{SFR}90}$ . This demonstrates the fueling of star-forming activity from newly accreted gas. Moreover, some stars are formed outside the star-forming radius, which indicates the growth of

the star-forming disk and the stellar disk. This qualitatively supports the picture of inside-out galaxy growth.

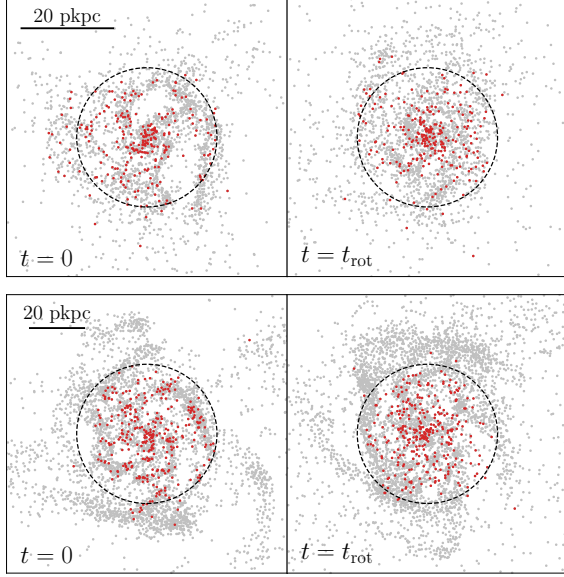


**Figure 10.** Cold gas moves towards inner galaxy to form stars. By projecting cold gas particles onto a 2D plane, each row shows a different galaxy: 43166 (*top*) and 37448 (*bottom*). The left and right column show the particle distribution before and after a rotation period respectively, i.e.,  $t = 0$  at  $z = 0.271$ , and  $t = t_{\text{rot}}$ . Each gray point represents a cold gas particle at both times. Each red point represents a cold gas particle at  $z = 0.271$  (*left*) that has turned into a star after a rotation period (*right*). Each dashed circle represents  $r_{\text{SFR}90}$  of each galaxy, defined at  $z = 0.271$ .

#### 4.5. Limitations of Ballistic Approximation

Using the ballistic approximation, both predicted inflow rate and mass-weighted average velocity generally agree with those from particle tracking to within a factor of two. In addition to the breakdown conditions of the ballistic approximation stated in Section 3.1, here we describe another cause of discrepancies between the two sets of inflow properties. We also discuss two caveats of comparing predictions from ballistic approximation to the outcome from the hydrodynamical calculations in EAGLE.

By following the gas particles in continuous timesteps, i.e., at multiple times for each galaxy, we find that feedback plays an important role. The ballistic approximation ignores the effect of feedback and predicts each particle trajectory by considering only gravity. But within a rotation period, feedback and winds expel some recently accreted gas particles to large radii. In the most extreme case (galaxy ID: 48386), not only does the feedback expel the newly accreted gas, but the feedback also

disrupts the star-forming region and disperses all of the cold gas.

The temperature increase of the cold gas particles also provides evidence for feedback; EAGLE implements the stellar feedback by stochastically heating particles to high temperature, known as the stochastic thermal feedback (Dalla Vecchia & Schaye 2008, 2012; Schaye et al. 2015). We focus on the change of temperature for particles that are predicted to reach the galaxy within a rotation period (by the ballistic approximation) but failed to do so (according to particle tracking). For the 11 central galaxies, around 50% of the particles that fail to be accreted have at least doubled their temperatures after a rotation period; the fraction varies among galaxies, from around 30% to 75%. For the most extreme case (galaxy ID: 48386), the particles have increased their temperatures by over 100 times to  $\sim 10^7$  K, indicating that the particles are strongly affected by feedback.

Because we identify inflowing gas using the location of particles after a rotation period, we have tracked the net inflow as the difference between the newly accreted gas and the gas expelled from the galaxy due to outflows. As some particles have once reached the star-forming region but have been expelled at later times due to feedback and winds, these particles explain the non-negligible fraction of predicted inflow particles that fail to be in the star-forming region after a rotation period (orange squares in Figure 7). In other words, whether or not a particle can accrete onto a galaxy and stay at the star-forming region without being expelled depends strongly on feedback. This phenomenon also qualitatively agrees with the results in Nelson et al. (2015) with AREPO and Correa et al. (2018b) with EAGLE; at  $z \leq 5$  and  $z \leq 2$ , feedback suppresses the accretion rates onto galaxies with halo masses below  $10^{12} M_{\odot}$ .

We emphasize that the comparison between the ballistic approximation and particle tracking only explores whether or how well the former resembles the hydrodynamical calculations in EAGLE. This comparison, however, has two caveats: there exist at least two factors that will result in different inflow properties deduced from different hydrodynamical simulations. First, because whether the gas can accrete onto galaxies is sensitive to feedback, this means the method of feedback implementation and the feedback strength will alter the inflow properties deduced from hydrodynamical simulations. Second, the inflow properties may be code-dependent. Nelson et al. (2013) (also see Nelson et al. 2015) study the cosmological gas accretion of  $\simeq 10^{11} M_{\odot}$  halos at  $z = 2$ . They find that compared to the SPH code GADGET-3, AREPO, a moving mesh code, produces an order of magnitude higher in hot accretion rate, but

a factor of two lower in cold accretion rate. Therefore, this demonstrates that the properties of inflowing gas are affected by the nature of the numerical approach.

## 5. INTERPRETING COLD GAS KINEMATICS FROM OBSERVATIONS

Previous sections have demonstrated the ubiquitousness of gas accretion onto the **EAGLE** galaxies. In contrast, observations rarely detect inflowing gas directly, as down-the-barrel galaxy observations can identify inflowing gas only if its Doppler shift can be distinguished from the ISM velocity dispersion. As a result, quasar sightline observations have provided the best observational probe of gas inflows, and these sightline observations have advanced our understanding of the gas kinematics of the CGM.

Quasar sightline observations have revealed important results regarding the cold gas kinematics of the CGM. First, through quasar sightlines that probe the CGM near galaxy major axes, observations often show that the cold CGM ( $\sim 10^4$  K), which is traced by low-ionization-state ions such as Mg II, corotates with the galaxy disks. Combining galaxy rotation curves and Mg II absorption profiles from quasar spectra, studies find cold absorbing gas that corotates with the disks at various redshifts: from low redshifts of  $z \sim 0.1$  (Kacprzak et al. 2011) and  $z \sim 0.2$  (Ho et al. 2017; Martin et al. 2019), to intermediate redshifts of  $z \sim 0.5$  (Kacprzak et al. 2010; Steidel et al. 2002). While similar types of data rarely exist at higher redshifts, there exists evidence suggesting that the cold gas shows similar kinematic properties as the lower redshift counterparts. Using other low-ionization-state ions (e.g., Zn II, Cr II), Bouché et al. (2013, 2016) study two galaxies at  $z = 2.3283$  and  $z = 0.9096$  respectively and detect corotating cold gas out to 26 pkpc and 12 pkpc. Second, for the observed corotating gas, the sightline impact parameters range from around 10 pkpc to even  $\sim 100$  pkpc. This exceeds the typical gas disk sizes of nearby galaxies measured from deep H I 21-cm observations,<sup>8</sup> e.g.,  $\sim 20$  pkpc in radius down to H I column density of  $\sim 5 \times 10^{19} \text{ cm}^{-2}$  for NGC 5023 and UGC 2082 from the HALOGAS survey (Heald et al. 2011; Kamphuis et al. 2013), and  $\sim 30$  pkpc in radius for NGC 891 down to  $10^{19} \text{ cm}^{-2}$  (Sancisi & Allen 1979; Oosterloo et al. 2007). Third, the low-ion absorption typically spans over  $100 \text{ km s}^{-1}$ . Despite the corota-

tion, a thin rotating disk fails to reproduce the broad velocity range. This problem demonstrates the need of additional components to describe the observed cold gas kinematics.

Inspired by these observations, we now observe the cold CGM kinematics in **EAGLE** using mock quasar sightlines. In this pilot study, limited by the galaxy sample size and resolution, our following discussion aims to encourage future work and focuses on one edge-on ( $i = 90^\circ$ ) galaxy. We will show that with this single galaxy, we can detect cold gas kinematics with characteristics similar to those detected in real quasar sightline observations. Therefore, this case study serves as motivation for future studies to ‘observe’ the cold CGM using **EAGLE** simulations with larger box sizes and a higher resolution, and to include the analysis of mock absorption line spectra.

Figure 11 shows the example galaxy to be studied in this Section. This Figure is similar to Figure 3, but in order to compare with cold gas traced by low-ionization-state ions, here we only show cold gas particles with  $T_{\text{gas}} \leq 3 \times 10^4$  K. Not only do the particles form a structure with a redshifted and a blueshifted side, which thereby indicates rotation, but the more extended particle distribution in the radial than in the  $Z$ -direction implies the rotating structure morphologically represents a disk (panel (a)). Furthermore, out to around 60 pkpc, the majority of the cold gas particles have angular momenta comparable to those required to be on circular orbits (panel (c)). This suggests a rotating disk radius of around 60 pkpc. Therefore, from both morphological and kinematical perspectives, this selected galaxy clearly has a giant, rotating cold gas disk.

Panel (d) shows that this extended gas disk is warped. By finding the net angular momentum vector at each concentric 10-pkpc shell, we calculate the angle between the net vector at the  $i$ -th shell and that at the innermost shell, or at the  $(i - 1)$ -th shell. The small but non-zero variations of both angles out to 60 pkpc implies that the disk plane changes orientation with radius, i.e., the gas disk is warped. Warped gas disks are also commonly found in hydrodynamical simulations, a result from cooling gas accreting onto galaxies and aligning its angular momentum vector with the central disks (e.g., Roškar et al. 2010; Stewart et al. 2011). In particular with the **EAGLE** simulations, Stevens et al. (2017) show that the angular momentum directions of both hot and cooling gas differ from that of the cooled gas by tens of degrees. This means that the gas particles precess as they cool, and their angular momenta align with the pre-existing cold gas in the galaxy. This leads to the formation of

<sup>8</sup> The observed H I disk size (diameter) depends on the depth of the observation; deeper observations measure H I emission down to a lower column density limit, resulting in a larger H I disk size. As an example, for NGC 5023, the H I diameter is 19 kpc at a column density limit of  $10^{20} \text{ cm}^{-2}$ , but the disk extends to about 27 kpc in diameter at  $2 \times 10^{19} \text{ cm}^{-2}$  (Kamphuis et al. 2013).

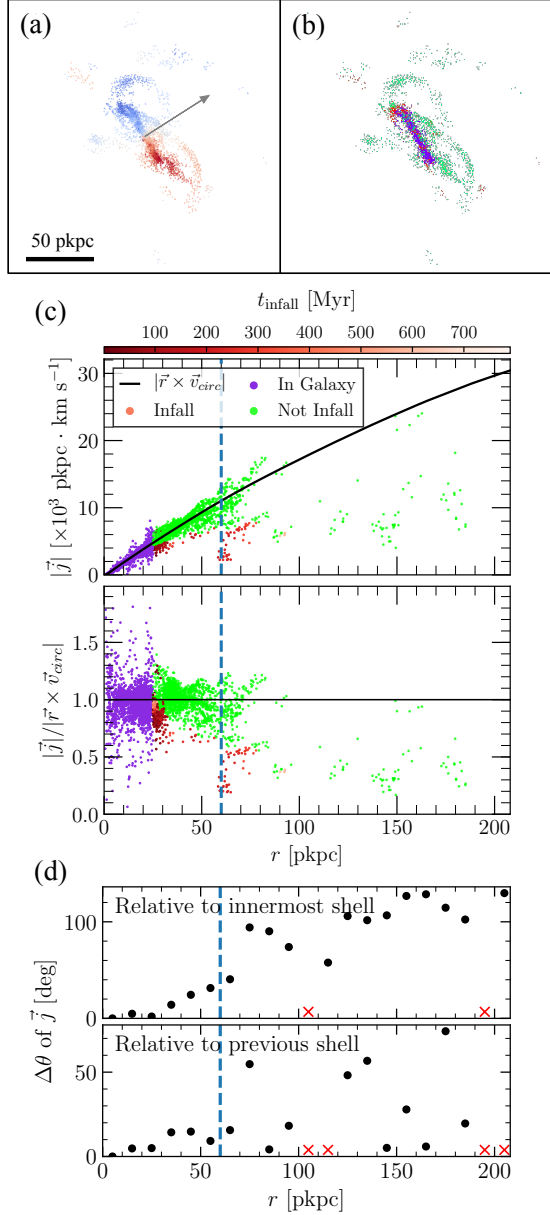


**Figure 11.** Distribution of cold gas particles ( $T_{\text{gas}} \leq 3 \times 10^4$  K) of a disk galaxy (ID: 37448) and the particle angular momenta. Panels (a) and (b) show cold gas particles projected onto 2D planes. Each particle is color-coded as in the top and middle row, respectively, of Figure 3. The gray arrow in panel (a) shows the direction of the net angular momentum of cold gas at the innermost 10-pkpc disk. Similar to the bottom row of Figure 3, panel (c) shows the specific angular momentum of each cold gas particle. By first finding the net angular momentum vector of each concentric 10-pkpc shell, panel (d) shows the angle between the net vector at each shell ( $i$ -th shell), and that at the innermost shell, or at the previous ( $(i-1)$ -th) shell. Red crosses indicate cold gas particles do not exist at the  $i$ -th shell (or at the  $(i-1)$ -th shell). The vertical dashed lines in panel (c) and (d) mark the radius of the cold gas disk of 60 pkpc.

an extended, warped gas disk, similar to our example galaxy in Figure 11.

In this section, first we describe how we generate the mock sightlines in Section 5.1. In Section 5.2, by measuring the mean LOS velocities along sightlines, we explore which sightlines can detect cold gas that corotates with the galaxy disk. Then in Section 5.3, we study how LOS velocity varies along sightlines, and we discuss the galaxy structures that can also produce velocity ranges comparable to those measured in real quasar sightline observations.

### 5.1. Creating Mock Quasar Sightlines

To create the mock quasar sightlines, first we define the disk plane of the galaxy. Within the innermost 10-pkpc of the galaxy, we calculate the net angular momentum vector of the cold gas and use this vector to define the disk plane. For a fixed galaxy inclination angle  $i$  (e.g.,  $i = 90^\circ$ ), we generate sightlines with impact parameter  $b$  between 10 pkpc and 100 pkpc and azimuthal angle<sup>9</sup>  $\alpha$  from  $0^\circ$  to  $90^\circ$ . Figure 12 illustrates the grid of sightlines relative to the galaxy major axis. Then for each combination of  $i$ ,  $b$ , and  $\alpha$ , we produce 12 LOSs by changing the location of the observer; each sightline runs along a different direction relatively to the simulation box, but as viewed from the ‘relocated’ observer, the sightlines still intersect the disk at the given  $i$ ,  $b$  and  $\alpha$ . Moreover, because in this work, we are interested in the kinematic signatures of cold gas within the halo, we create each LOS to extend only to the galaxy virial radius  $r_{\text{vir}}$ .

Analogous to observations, which trace cold gas using low ions (e.g., Mg II, Si II, Fe II), we redefine the cold gas temperature cutoff as  $3 \times 10^4$  K (see Section 2.2). We use yt (Turk et al. 2011) to convert the cold gas particle fields to grid-based fluid quantities. We extract the cold gas density and velocity at cells intersected by each sightline. Then we calculate the mean LOS velocity, and we explore how the LOS velocity changes along sightlines in Section 5.2 and 5.3 respectively.

### 5.2. CGM Corotation with Galactic Disk

We pose the question of which sightlines can detect cold gas that corotates with the inner galaxy disk. Using the mock sightlines that probe the edge-on galaxy, for each of the 12 LOS at different  $b$  and  $\alpha$ , we calculate the mean LOS velocity (column density weighted). If

<sup>9</sup> Measured from the galaxy center, azimuthal angle  $\alpha$  is the angular separation of the sightline from the galaxy major axis. A sightline at  $\alpha = 0^\circ$  lies on the major axis, whereas a sightline at  $\alpha = 90^\circ$  lies on the minor axis.



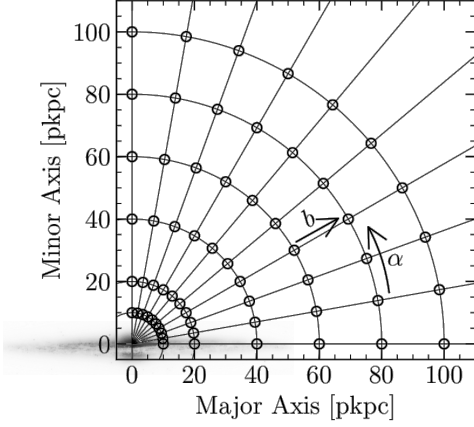


**Figure 12.** Grid of mock sightlines relative to galaxy major axis. The origin of the coordinate grid represents the center of the galaxy. Each circle represents the position of a sightline.

this mean LOS velocity has the same sign as the disk rotation and is at least  $10 \text{ km s}^{-1}$  away from the galaxy systemic velocity, then we classify the LOS as detecting corotating gas. The latter criterion prevents misassigning cold gas that moves randomly within thermal and turbulent velocity as corotating.

Before discussing the detection of cold corotating gas, we note that not all LOS intersect cold gas. The top panel of Figure 13 shows that among the 12 LOS per  $b$ - $\alpha$  combination, the number of LOS that intersects cold gas decreases with increasing  $b$  and  $\alpha$ . This can be explained by the decreasing cold gas density when the radial separation from the galaxy center increases (e.g., see the cold gas distribution in Figure 11(a)).

Using the sightlines that have intersected cold gas, we explore what ranges of  $b$  and  $\alpha$  can detect corotating gas. At each  $b$ - $\alpha$  combination, first we find the number of LOS that intersects cold gas  $N_{\text{cold}}$  and the number of LOS that detects corotating cold gas  $N_{\text{cr}}$ . With binomial statistics (Gehrels 1986), we calculate the  $1\sigma$  lower limit of the rate of detecting corotating cold gas  $p_{\text{cr},1l}$ . The bottom panel of Figure 13 isolates the sightlines in the  $b$ - $\alpha$  plane with  $p_{\text{cr},1l} > 0.5$ ; within  $1\sigma$ -level of confidence, it is unlikely that these sightlines have detected randomly moving cold gas. This is because with random gas motion, sightlines will detect corotation at half of the times, and the probability of detecting corotating gas at one sightline will be  $p = 0.5$ . This probability, however, is excluded with  $1\sigma$ -level of confidence if  $p_{\text{cr},1l} > 0.5$ . Then, among these sightlines in the  $b$ - $\alpha$  plane, we also ask the following question: *if* the gas moves randomly, what is the probability of having  $\geq N_{\text{cr}}$  LOS that detect corotating gas among the  $N_{\text{cold}}$  LOS. We show this probability using the color scale in the bottom panel

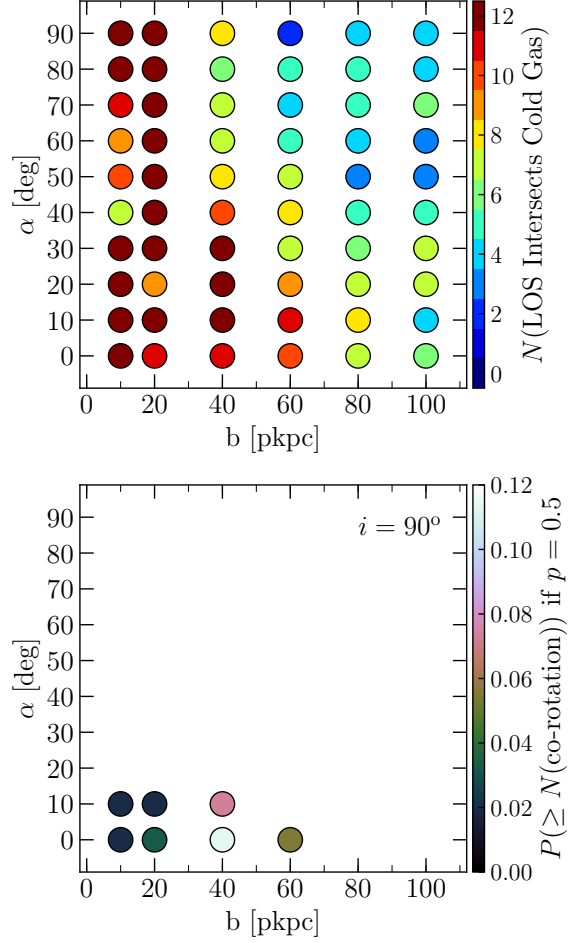


**Figure 13.** Locations of sightlines that detect corotating cold gas around an edge-on ( $i = 90^\circ$ ) galaxy (galaxy ID: 37448). (top) Number of LOS (out of 12) that intersects cold gas with  $T_{\text{gas}} \leq 3 \times 10^4 \text{ K}$ . Fewer LOS at large  $b$  and high  $\alpha$  intersect cold gas within the galaxy virial radius. (bottom) This panel only shows the sightlines along which we rule out random gas motion at  $1\sigma$ -level of confidence. Sightlines at  $\alpha = 0^\circ$  and  $10^\circ$  detect corotating cold gas out to 60 pkpc and 40 pkpc respectively. In particular, *if* the gas had moved randomly, then the probabilities of detecting  $\geq N_{\text{cr}}$  LOS with corotating cold gas at  $\alpha = 0^\circ$  and  $10^\circ$  within  $b = 20$  pkpc would lie below 5% (indicated by the colors). This implies that these sightlines have detected corotating cold gas.

of Figure 13. Among the selected  $b$ - $\alpha$  locations, the chances of detecting  $\geq N_{\text{cr}}$  sightlines with corotating gas lie below 12%. In particular, at  $b = 10$  pkpc and 20 pkpc, the probabilities at both  $\alpha = 0^\circ$  and  $10^\circ$  lie below 5%. Thus, the calculation suggests that sightlines shown in the lower panel of Figure 13, i.e., sightlines at  $\alpha = 0^\circ$  and  $10^\circ$  out to 60 pkpc and 40 pkpc, respectively, have unlikely intersected randomly moving gas. In other words, these sightlines can detect corotating cold gas.

Our edge-on galaxy example demonstrates that quasar sightlines are more likely to detect corotating cold gas near the galaxy disk plane: at sightlines with  $b \leq 60$  pkpc and low  $\alpha$  of  $\leq 10^\circ$ . This can be naturally explained by sightlines intersecting the rotating gas disk as shown in Figure 11(a). Since real quasar sightline observations often detect corotating cold gas along sightlines near the galaxy major axes, our example suggests that these sightlines have likely intersected cold gas disks that extend beyond the optical disks.

While we use one **EAGLE** galaxy to demonstrate the possibility of detecting corotating cold gas using mock quasar sightlines, the presence of rotating structures, which can give rise to corotating gas detection, is not unique to this galaxy. Figure 14 shows the cold gas distribution of the remaining 10 central galaxies, and we color each particle by its projected LOS velocity. Although the spatial distribution of particles indicates that not all galaxies have thin-disk-like morphologies, at least half of the galaxies have cold gas structures that show signs of rotation, i.e., an approaching side and a receding side. Rotating gas structures are not only common among our selected galaxies. Simulated galaxies with halo mass  $\gtrsim 10^{11} M_\odot$  from the **FIRE** project also show clear signs of rotation, even though the gas distribution is not morphologically ‘disky’ (El-Badry et al. 2018). Hence, sightlines through all these galaxies may also detect corotating cold gas as in our example, and this may imply that the corotation detection is not a rare phenomenon.

### 5.3. Velocity Range Along LOS

Quasar sightline observations often detect broad LOS velocity ranges that cannot be explained by a thin rotating disk model. Therefore, using our example galaxy that has an extended rotating disk, we investigate the velocity ranges that this galaxy can produce.<sup>10</sup> By examining how LOS velocity varies along different sightlines, we discuss the resultant velocity ranges that can possibly be created by different gas structures.

We choose individual sightlines that intersect different components of the cold gas structure: (1) the thin disk: at small  $b$  and along the galaxy major axis ( $\alpha = 0^\circ$ ), (2) the thick disk: at small  $b$  and at least several kpc above the disk plane (e.g.,  $\alpha = 20^\circ$ ), and (3) a gas stream. Specifically for our edge-on galaxy example, a sightline

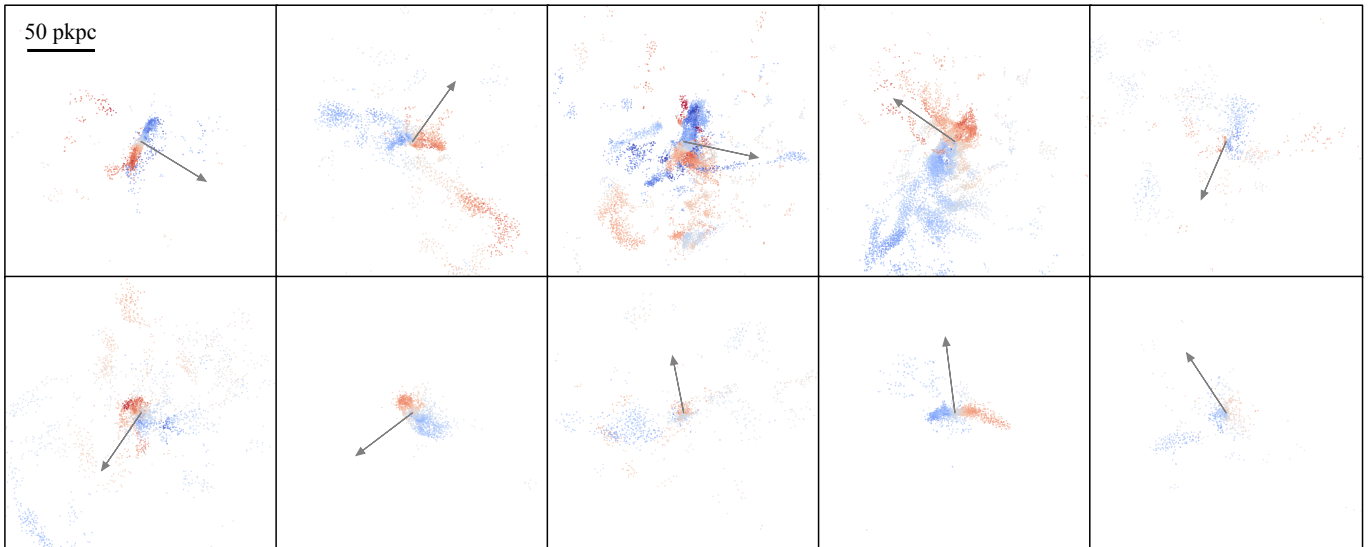
that intersects the disk midplane represents the thin disk component. Since **EAGLE** imposes a temperature floor of 8000 K to prevent metal-rich gas particles from cooling to very cold, interstellar gas (Schaye et al. 2015; Crain et al. 2015), this sets a minimum disk height, considerably larger than the physical scale height for observed edge-on galaxies (de Grijs 1998; Kregel et al. 2002). As a result, **EAGLE** cannot produce very flat galaxies (also see Lagos et al. (2018) for a related discussion). We select our sightline that intersects the thick disk component  $\sim 10$  pkpc above the disk midplane, avoiding the ‘unresolved’ thin disk. We call this the ‘thick disk’ component also because the 10-kpc thickness is comparable to that of the modeled rotating gas disks (tens of kpc tall) in explaining the measured CGM kinematics (e.g., Steidel et al. 2002; Ho et al. 2017; Ho & Martin 2019).

Figure 15 shows the variation of LOS velocity and cold gas density along each of the three sightlines. Along the path of each sightline,  $D_{\text{los}} = 0$  pkpc separates the near side and the far side of the edge-on disk. Although our sightlines extend to  $r_{\text{vir}}$ , we only plot  $|D_{\text{los}}| \leq 80$  pkpc. Beyond this pathlength, the sightlines rarely intersect any cold gas within  $r_{\text{vir}}$ . Even if cold gas is intersected, it has order-of-magnitudes lower density than the intersected cold gas within  $|D_{\text{los}}| \leq 80$  pkpc. In addition, a positive LOS velocity indicates that it has the same sign as the disk angular momentum, i.e., the intersected cold gas corotates with the galaxy disk. For each of the three sightlines that intersect the three structures, the LOS velocities stay positive. This indicates that the intersected cold gas always shares the same sense of rotation as the inner galaxy disk. In the following, we briefly discuss the velocity variation along individual sightlines.

First, the sightline that intersects the thin disk detects the broadest LOS velocity range. The LOS velocity  $v_{\text{los}}$  reaches  $210 \text{ km s}^{-1}$  at  $D_{\text{los}} = 0$ , where the cold gas density also peaks (red line in Figure 15). The large  $v_{\text{los}}$  is produced by the circular motion of the gas on the disk, and the rotation velocity vector is tangent to the sightline at  $D_{\text{los}} = 0$ . Increasing  $|D_{\text{los}}|$  then reduces the magnitude of  $v_{\text{los}}$  significantly, because the LOS no longer runs in parallel with the rotation velocity vector. Along this sightline, since the LOS velocity varies from around  $30 \text{ km s}^{-1}$  to  $210 \text{ km s}^{-1}$ , this sightline can detect a broad LOS velocity range of  $180 \text{ km s}^{-1}$ .

Second, the sightline that intersects the thick disk component produces a narrower velocity range. The LOS velocity reaches maxima of around  $70 \text{ km s}^{-1}$  and  $110 \text{ km s}^{-1}$  at the near and the far side of the disk respectively, and the velocity minimum along the sightline is around  $30 \text{ km s}^{-1}$  (orange line in Figure 15). The den-

<sup>10</sup> In spectroscopic observations, whether or not the cold gas can be detected and the measured velocity ranges depend on the equivalent widths of the absorption systems and the spectroscopic sensitivity. Our discussion focuses on the velocity ranges that can be produced by the cold gas, and we implicitly assume that all cold gas can be detected.



**Figure 14.** Projected LOS velocities of cold gas particles with  $T_{\text{gas}} \leq 3 \times 10^4$  K. Each panel projects the cold gas particles of each central galaxy onto a 2D plane. Every particle is color-coded by its projected LOS velocity. Red and blue colors represent redshifted and blueshifted cold gas particles respectively, and we use the same velocity scale as in the top row of Figure 3. The gray arrow shows the direction of the net angular momentum of the cold gas, which is measured within an aperture of 10-pkpc from the galaxy center. More than half of the galaxies show signs of rotation. Each panel has the same spatial scale of  $200 \text{ pkpc} \times 200 \text{ pkpc}$ .

sity peaks at the two locations of the velocity maxima, which indicates that the thick disk component does not comprise a uniform disk. This is evident from the gas distribution in Figure 3, which shows the gas having spiral structures instead of being a solid disk. Since this sightline detects LOS velocity that varies from around  $30 \text{ km s}^{-1}$  to a maximum of  $110 \text{ km s}^{-1}$ , the velocity range reaches  $80 \text{ km s}^{-1}$ , which significantly exceeds the thermal linewidth.

As for the sightline that intersects a gas stream, only discrete sections along the sightline have intersected cold gas. The sightline intersects the gas stream at around  $D_{\text{los}} = -40 \text{ pkpc}$  (yellow line in Figure 15). At the far side of the disk of  $D_{\text{los}} = 20 \text{ pkpc}$ , the sightline intersects cold gas whose density is of 100 times lower. The higher density gas stream produces LOS velocities from around  $30 \text{ km s}^{-1}$  to a maximum of  $100 \text{ km s}^{-1}$ . Therefore, this sightline produces a LOS velocity range comparable to that of the thick disk component.

Using the three cases of our example edge-on galaxy, we have demonstrated that velocity ranges of over  $100 \text{ km s}^{-1}$  in observations can be produced by a sightline that intersects a thin rotating disk edge-on. Sightlines that intersect the thick disk component or a gas stream can detect LOS velocity ranges that are significantly broader than the thermal linewidth. All these gas structures likely contribute to the broad line profiles in real observations, especially because the observed pro-

files broadened by instrumental resolution are expected to consist of multiple velocity components.

However, we emphasize that while the three example sightlines can produce broad velocity ranges in principle, such sightlines are extremely rare. As a result, they cannot explain the large number of broad absorption systems observed. Moreover, the observed velocity range of the absorption depends on the column density and thereby the ionization state of the gas, which is beyond the scope of this paper. Therefore, in the future, we will conduct the ionization analysis and use mock sightlines to study the absorption line profiles of different ionic species. This will provide us deeper insight into the circumgalactic gas kinematics measured in quasar sightline observations.

## 6. SUMMARY AND CONCLUSIONS

Galaxies grow and fuel star formation by accreting gas, yet direct observation of gas inflows onto galaxies remains sparse. In this pilot study, we have studied the properties of cold inflowing gas around EAGLE galaxies at  $z = 0.27$ . We have identified the cold inflowing gas using two methods: (i) a ballistic approximation that calculates the trajectories of particles moving under gravity, and then predicts which particles accrete onto the inner galaxy within a rotation period, and (ii) tracking particles through the same time interval in EAGLE, which includes full hydrodynamic calculations. We have compared the two sets of deduced inflow properties and discussed the limitations of the ballistic approximation.

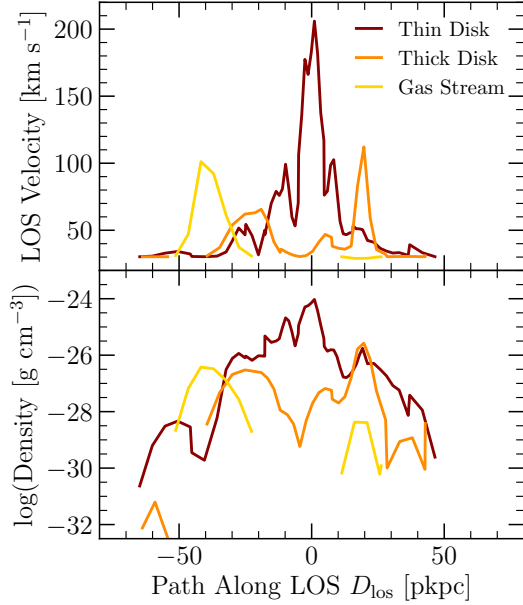


**Figure 15.** Variation of LOS velocity and cold gas density along selected sightlines of the example edge-on galaxy (galaxy ID: 37448). The top and the bottom panel show how the LOS velocity and cold gas density vary along sightlines that individually intersect three structural components: a thin disk (red), a thick disk (orange), and a gas stream (yellow). A positive LOS velocity indicates the LOS velocity has the same sign as the disk angular momentum.  $D_{\text{los}} = 0$  separates the near side and the far side of the galaxy disk with respect to the observer. Any discontinuity along  $D_{\text{los}}$  indicates that cold gas is not intersected by that section of the sightline. We only show  $|D_{\text{los}}| \leq 80$  pkpc along the path, beyond which all three sightlines rarely intersect any cold gas.

To gain insight into understanding cold gas kinematics measured from quasar sightline observations, we have probed the cold CGM ( $\sim 10^4$  K) using mock quasar sightlines. Our analysis has focused on the CGM corotation with the galactic disk, as well as the velocity ranges produced by different galaxy structures.

Using either the ballistic approximation or particle tracking, we find that the galaxies typically have low inflow speeds of around  $20 \text{ km s}^{-1}$  to  $60 \text{ km s}^{-1}$ . The mass inflow rates deduced from the two methods agree to within a factor of two, and the ballistic approximation often over-estimates. We have attributed the major cause of the discrepancy to feedback, which has removed the newly accreted gas or can even disrupt the star-forming regions. In other words, feedback reduces the overall amount of cold gas accreted and thereby suppresses the mass inflow rates. Nevertheless, the mass inflow rates are generally comparable to the galaxy SFRs. This suggests that the cold inflowing gas plausibly sus-

tains the galaxy star formation activities and thereby prolong the disk lifetimes.

Inspired by recent observational measurements of cold gas kinematics along quasar sightlines, we have used mock quasar sightlines to probe the cold gas within  $r_{\text{vir}}$  around a selected **EAGLE** galaxy. This galaxy has an extended cold gas disk, and the measurements of its cold gas kinematics share similar characteristics as in sightline observations. This motivates future work using larger simulation boxes with a higher resolution to ‘observe’ the cold gas kinematics in detail.

We have posed the question of which sightlines can detect cold gas that corotates with the inner galaxy disk. By viewing the selected **EAGLE** galaxy edge-on, we have found that sightlines with azimuthal angles of  $\alpha = 0^\circ$  and  $10^\circ$  can detect corotating cold gas out to 60 pkpc and 40 pkpc respectively. Since quasar sightline observations often detect corotating cold gas near the galaxy major axes, our results suggest it is possible that the observed sightlines have intersected cold gas disks that extend beyond the optical disks.

Because quasar sightline observations also often detect broad velocity profiles, we have explored whether sightlines that individually intersect a thin disk component, a thick disk component (i.e., above the disk plane), and a gas stream can produce comparable velocity ranges. We have demonstrated that sightlines intersecting these three gas components can produce velocity ranges of over  $70 \text{ km s}^{-1}$ , significantly broader than the thermal linewidth. All these structures possibly contribute to the broad line profiles in observational measurements, especially because the observed line profiles are expected to consist of multiple velocity components.

In the future, we will use **EAGLE** simulations with large box sizes and higher resolutions to study cold gas kinematics. With larger cosmological volumes, we can increase the sampling size of galaxies. This will produce better statistics on the probabilities of detecting corotating cold gas along sightlines and finding galaxies with extended cold gas disks. Using simulations with better resolution will allow us to generate high resolution, mock absorption line spectra and compare them to quasar sightline measurements. This will allow us to interpret quasar sightline observations using **EAGLE** simulations and thereby gain insight into understanding the measured cold gas kinematics.

We thank the referee for the thoughtful and detailed comments that improved the manuscript. We gratefully acknowledge Joop Schaye for the inspirational discussions on both the technical and science aspects of this paper. We thank Marie Lau and Michael Lipatov for



their suggestions on the manuscript. We also thank Suoqing Ji and Nathan Goldbaum for the helpful discussion regarding the use of `yt`. Material presented in this paper is based in part upon work supported by the National Science Foundation under Grant No. 1817125. We acknowledge the Virgo Consortium for making their

simulation data available. The **EAGLE** simulations were performed using the DiRAC-2 facility at Durham, managed by the ICC, and the PRACE facility Curie based in France at TGCC, CEA, Bruyères-le-Châtel. This work has made use of the `yt` astrophysics analysis and visualization tool ([Turk et al. 2011](#)).

## REFERENCES

- Bahé, Y. M., Crain, R. A., Kauffmann, G., et al. 2016, *MNRAS*, 456, 1115
- Bigiel, F., Leroy, A., Walter, F., et al. 2008, *AJ*, 136, 2846
- Bigiel, F., Leroy, A. K., Walter, F., et al. 2011, *ApJL*, 730, L13
- Boselli, A., Gavazzi, G., Donas, J., & Scodreggio, M. 2001, *AJ*, 121, 753
- Bouché, N., Hohensee, W., Vargas, R., et al. 2012, *MNRAS*, 426, 801
- Bouché, N., Murphy, M. T., Kacprzak, G. G., et al. 2013, *Science*, 341, 50
- Bouché, N., Dekel, A., Genzel, R., et al. 2010, *ApJ*, 718, 1001
- Bouché, N., Finley, H., Schroetter, I., et al. 2016, *ApJ*, 820, 121
- Bowen, D. V., Chelouche, D., Jenkins, E. B., et al. 2016, *ApJ*, 826, 50
- Brinchmann, J., Charlot, S., White, S. D. M., et al. 2004, *MNRAS*, 351, 1151
- Brook, C. B., Governato, F., Roškar, R., et al. 2011, *MNRAS*, 415, 1051
- Bryan, G. L., & Norman, M. L. 1998, *ApJ*, 495, 80
- Coil, A. L., Blanton, M. R., Burles, S. M., et al. 2011, *ApJ*, 741, 8
- Cool, R. J., Moustakas, J., Blanton, M. R., et al. 2013, *ApJ*, 767, 118
- Correa, C. A., Schaye, J., van de Voort, F., Duffy, A. R., & Wyithe, J. S. B. 2018a, *MNRAS*, 478, 255
- Correa, C. A., Schaye, J., Wyithe, J. S. B., et al. 2018b, *MNRAS*, 473, 538
- Crain, R. A., Schaye, J., Bower, R. G., et al. 2015, *MNRAS*, 450, 1937
- Crain, R. A., Bahé, Y. M., Lagos, C. d. P., et al. 2017, *MNRAS*, 464, 4204
- Dalla Vecchia, C., & Schaye, J. 2008, *MNRAS*, 387, 1431
- . 2012, *MNRAS*, 426, 140
- Danovich, M., Dekel, A., Hahn, O., Ceverino, D., & Primack, J. 2015, *MNRAS*, 449, 2087
- Danovich, M., Dekel, A., Hahn, O., & Teyssier, R. 2012, *MNRAS*, 422, 1732
- Davé, R., Finlator, K., & Oppenheimer, B. D. 2012, *MNRAS*, 421, 98
- Davis, M., Efstathiou, G., Frenk, C. S., & White, S. D. M. 1985, *ApJ*, 292, 371
- de Grijs, R. 1998, *MNRAS*, 299, 595
- Dekel, A., & Birnboim, Y. 2006, *MNRAS*, 368, 2
- Diamond-Stanic, A. M., Coil, A. L., Moustakas, J., et al. 2016, *ApJ*, 824, 24
- Dolag, K., Borgani, S., Murante, G., & Springel, V. 2009, *MNRAS*, 399, 497
- El-Badry, K., Quataert, E., Wetzel, A., et al. 2018, *MNRAS*, 473, 1930
- Fall, S. M., & Efstathiou, G. 1980, *MNRAS*, 193, 189
- Fox, A. J., Wakker, B. P., Barger, K. A., et al. 2014, *ApJ*, 787, 147
- Furlong, M., Bower, R. G., Theuns, T., et al. 2015, *MNRAS*, 450, 4486
- Gehrels, N. 1986, *ApJ*, 303, 336
- Heald, G., Józsa, G., Serra, P., et al. 2011, *A&A*, 526, A118
- Heckman, T. M., Alexandroff, R. M., Borthakur, S., Overzier, R., & Leitherer, C. 2015, *ApJ*, 809, 147
- Ho, S. H., & Martin, C. L. 2019, arXiv e-prints, arXiv:1901.11182
- Ho, S. H., Martin, C. L., Kacprzak, G. G., & Churchill, C. W. 2017, *ApJ*, 835, 267
- Kacprzak, G. G., Churchill, C. W., Barton, E. J., & Cooke, J. 2011, *ApJ*, 733, 105
- Kacprzak, G. G., Churchill, C. W., Ceverino, D., et al. 2010, *ApJ*, 711, 533
- Kacprzak, G. G., Churchill, C. W., & Nielsen, N. M. 2012, *ApJL*, 760, L7
- Kacprzak, G. G., Muzahid, S., Churchill, C. W., Nielsen, N. M., & Charlton, J. C. 2015, *ApJ*, 815, 22
- Kacprzak, G. G., Martin, C. L., Bouché, N., et al. 2014, *ApJL*, 792, L12
- Kamphuis, P., Rand, R. J., Józsa, G. I. G., et al. 2013, *MNRAS*, 434, 2069
- Kennicutt, Jr., R. C. 1998, *ARA&A*, 36, 189
- Kennicutt, Jr., R. C., Tamblyn, P., & Congdon, C. E. 1994, *ApJ*, 435, 22

- Kereš, D., Katz, N., Fardal, M., Davé, R., & Weinberg, D. H. 2009, *MNRAS*, 395, 160
- Kereš, D., Katz, N., Weinberg, D. H., & Davé, R. 2005, *MNRAS*, 363, 2
- Kimm, T., Devriendt, J., Slyz, A., et al. 2011, *ArXiv e-prints*, arXiv:1106.0538
- Kregel, M., van der Kruit, P. C., & de Grijs, R. 2002, *MNRAS*, 334, 646
- Lagos, C. d. P., Schaye, J., Bahé, Y., et al. 2018, *MNRAS*, 476, 4327
- Lagos, C. d. P., Theuns, T., Stevens, A. R. H., et al. 2017, *MNRAS*, 464, 3850
- Lagos, C. d. P., Crain, R. A., Schaye, J., et al. 2015, *MNRAS*, 452, 3815
- Leroy, A. K., Walter, F., Brinks, E., et al. 2008, *AJ*, 136, 2782
- Leroy, A. K., Walter, F., Sandstrom, K., et al. 2013, *AJ*, 146, 19
- Martin, C. L. 1999, *ApJ*, 513, 156
- Martin, C. L., Ho, S. H., Kacprzak, G. G., & Churchill, C. W. 2019, *arXiv e-prints*, arXiv:1901.09123
- Martin, C. L., Shapley, A. E., Coil, A. L., et al. 2012, *ApJ*, 760, 127
- McAlpine, S., Helly, J. C., Schaller, M., et al. 2016, *Astronomy and Computing*, 15, 72
- Mo, H. J., Mao, S., & White, S. D. M. 1998, *MNRAS*, 295, 319
- Moustakas, J., Coil, A. L., Aird, J., et al. 2013, *ApJ*, 767, 50
- Nelson, D., Genel, S., Vogelsberger, M., et al. 2015, *MNRAS*, 448, 59
- Nelson, D., Vogelsberger, M., Genel, S., et al. 2013, *MNRAS*, 429, 3353
- Nielsen, N. M., Churchill, C. W., Kacprzak, G. G., Murphy, M. T., & Evans, J. L. 2015, *ApJ*, 812, 83
- Oosterloo, T., Fraternali, F., & Sancisi, R. 2007, *AJ*, 134, 1019
- Oppenheimer, B. D., & Schaye, J. 2013, *MNRAS*, 434, 1043
- Peng, Y.-j., Lilly, S. J., Kovač, K., et al. 2010, *ApJ*, 721, 193
- Pichon, C., Pogosyan, D., Kimm, T., et al. 2011, *MNRAS*, 418, 2493
- Prochaska, J. X., Werk, J. K., Worseck, G., et al. 2017, *ApJ*, 837, 169
- Putman, M. E., Peek, J. E. G., & Jounge, M. R. 2012, *ARA&A*, 50, 491
- Rahman, N., Bolatto, A. D., Xue, R., et al. 2012, *ApJ*, 745, 183
- Roberts, M. S. 1963, *ARA&A*, 1, 149
- Robertson, B. E., & Kravtsov, A. V. 2008, *ApJ*, 680, 1083
- Roškar, R., Debattista, V. P., Brooks, A. M., et al. 2010, *MNRAS*, 408, 783
- Rubin, K. H. R., Prochaska, J. X., Koo, D. C., & Phillips, A. C. 2012, *ApJL*, 747, L26
- Rudie, G. C., Steidel, C. C., Trainor, R. F., et al. 2012, *ApJ*, 750, 67
- Rupke, D. S., Veilleux, S., & Sanders, D. B. 2005, *ApJS*, 160, 115
- Saintonge, A., Kauffmann, G., Kramer, C., et al. 2011, *MNRAS*, 415, 32
- Sancisi, R., & Allen, R. J. 1979, *A&A*, 74, 73
- Schaye, J., & Dalla Vecchia, C. 2008, *MNRAS*, 383, 1210
- Schaye, J., Dalla Vecchia, C., Booth, C. M., et al. 2010, *MNRAS*, 402, 1536
- Schaye, J., Crain, R. A., Bower, R. G., et al. 2015, *MNRAS*, 446, 521
- Schiminovich, D., Catinella, B., Kauffmann, G., et al. 2010, *MNRAS*, 408, 919
- Schmidt, M. 1963, *ApJ*, 137, 758
- Sommer-Larsen, J. 1991, *MNRAS*, 249, 368
- Springel, V. 2005, *MNRAS*, 364, 1105
- Springel, V., White, S. D. M., Tormen, G., & Kauffmann, G. 2001, *MNRAS*, 328, 726
- Steidel, C. C., Kollmeier, J. A., Shapley, A. E., et al. 2002, *ApJ*, 570, 526
- Steidel, C. C., Rudie, G. C., Strom, A. L., et al. 2014, *ApJ*, 795, 165
- Stevens, A. R. H., Lagos, C. d. P., Contreras, S., et al. 2017, *MNRAS*, 467, 2066
- Stewart, K. R., Brooks, A. M., Bullock, J. S., et al. 2013, *ApJ*, 769, 74
- Stewart, K. R., Kaufmann, T., Bullock, J. S., et al. 2011, *ApJ*, 738, 39
- Stewart, K. R., Maller, A. H., Oñorbe, J., et al. 2017, *ApJ*, 843, 47
- Stocke, J. T., Keeney, B. A., Danforth, C. W., et al. 2013, *ApJ*, 763, 148
- Teklu, A. F., Remus, R.-S., Dolag, K., et al. 2015, *ApJ*, 812, 29
- Trayford, J. W., Theuns, T., Bower, R. G., et al. 2016, *MNRAS*, 460, 3925
- . 2015, *MNRAS*, 452, 2879
- Tumlinson, J., Peebles, M. S., & Werk, J. K. 2017, *ARA&A*, 55, 389
- Turk, M. J., Smith, B. D., Oishi, J. S., et al. 2011, *The Astrophysical Journal Supplement Series*, 192, 9
- Turner, M. L., Schaye, J., Crain, R. A., et al. 2017, *MNRAS*, 471, 690
- Turner, M. L., Schaye, J., Steidel, C. C., Rudie, G. C., & Strom, A. L. 2014, *MNRAS*, 445, 794
- van de Voort, F., Schaye, J., Booth, C. M., Haas, M. R., & Dalla Vecchia, C. 2011, *MNRAS*, 414, 2458

- van den Bergh, S. 1962, AJ, 67, 486
- Werk, J. K., Prochaska, J. X., Tumlinson, J., et al. 2014, ApJ, 792, 8
- Worthey, G., Dorman, B., & Jones, L. A. 1996, AJ, 112, 948
- Zheng, Y., Putman, M. E., Peek, J. E. G., & Joung, M. R. 2015, ApJ, 807, 103
- Zschaechner, L. K., Rand, R. J., Heald, G. H., Gentile, G., & Józsa, G. 2012, ApJ, 760, 37

## APPENDIX

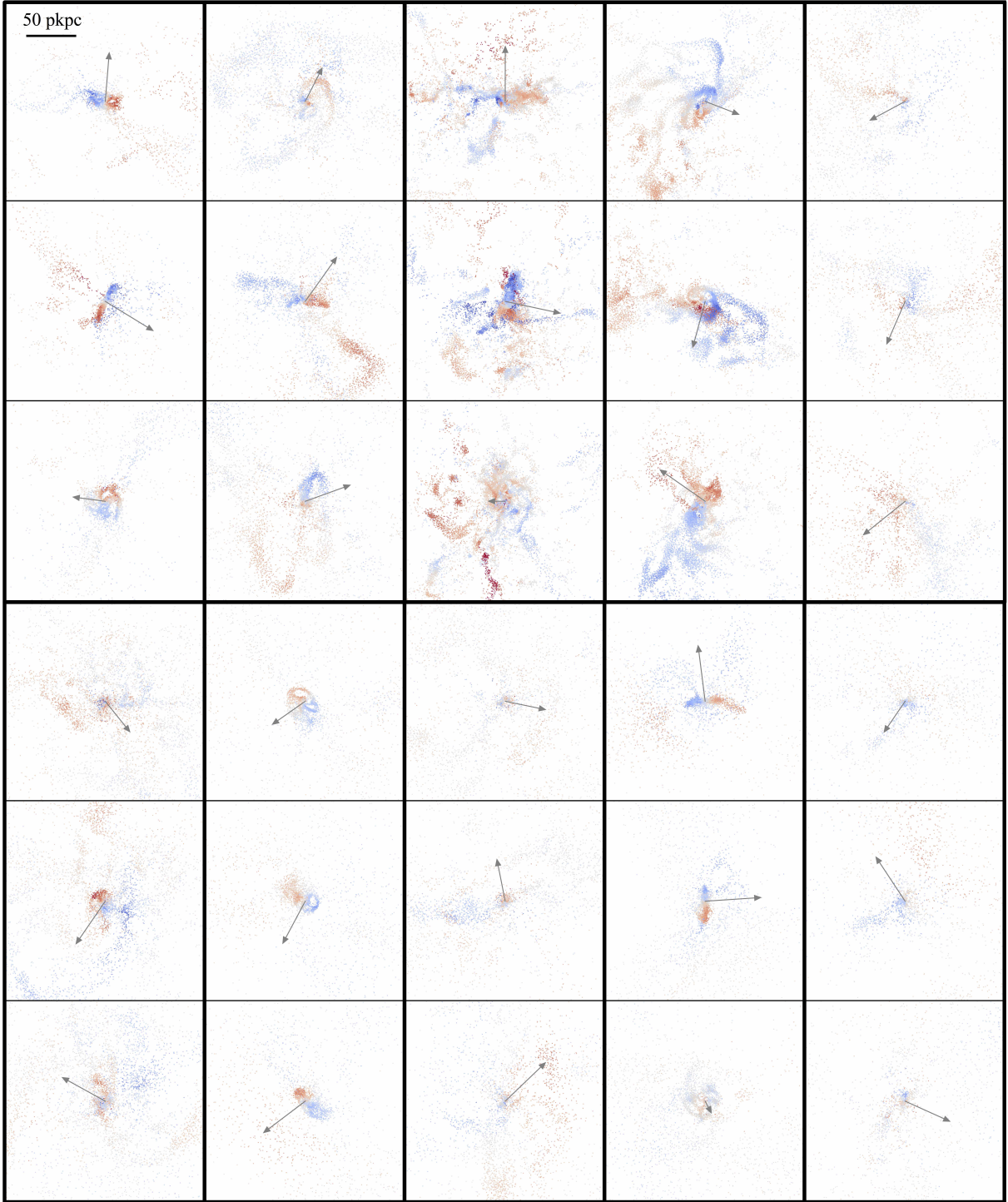


**Figure 16.** Particle projection plots showing the projected LOS velocities of cold gas particles ( $T_{\text{gas}} \leq 2.5 \times 10^5$  K). Each particle is color-coded by its projected velocity, and we use the same velocity scale as in the top row of Figure 3. This figure follows the same format as in Figure 4. Each galaxy occupies 3 rows  $\times$  1 column, enclosed by the thick black lines. For individual galaxies, from top to bottom, each panel represents the cut in  $x$ ,  $y$  and  $z$  plane respectively. The side length of each panel is 200 pkpc. The plotted central galaxies are ordered in decreasing stellar masses, from left to right, and top to bottom.